JGR Solid Earth

RESEARCH ARTICLE
10.1029/2022JB025798

Local Earthquake Seismic Tomography Reveals the Link Between Crustal Structure and Volcanism in Tenerife (Canary Islands)

Ivan Koulakov[1,2], Luca D'Auria[3,4], Janire Prudencio[5,6], Iván Cabrera-Pérez[3], José Barrancos[3,4], Germán D. Padilla[3,4], Sergei Abramenkov[1,7], Nemesio M. Pérez[3,4], and Jesús M. Ibáñez[5,6]

[1]Trofimuk Institute of Petroleum Geology and Geophysics SB RAS, Novosibirsk, Russia, [2]Institute of the Earth's Crust SB RAS, Lermontova 128, Irkutsk, Russia, [3]Instituto Volcanológico de Canarias (INVOLCAN), Calle Álvaro Martín Díaz, Tenerife, Spain, [4]Instituto Tecnológico y de Energías Renovables (ITER), Polígono Industrial de Granadilla s/n, Tenerife, Spain, [5]Department of Theoretical Physics and Cosmos, Science Faculty, Avd. Fuenteneueva s/n, University of Granada, Granada, Spain, [6]Andalusian Institute of Geophysics, Campus de Cartuja, University of Granada, C/Profesor Clavera 12, Granada, Spain, [7]Novosibirsk State University, Novosibirsk, Russia

Abstract Volcanic activity on Tenerife Island is extremely diverse. Three radial rift zones are characterized by cinder cones from basaltic fissure eruptions. A triple junction in central Tenerife exhibits a complex of merged, predominantly phonolitic, stratovolcanoes. The Las Cañadas caldera and widespread ignimbrite deposits reveal high explosive potential. We investigated the crustal and upper mantle structure beneath Tenerife using local earthquake data recorded by two dense seismic networks on the island. For our tomographic inversion, we selected >130,000 *P*- and *S*-wave arrivals from ~6,300 events that occurred during seismic unrests in 2004–2005 and 2017–2021. Synthetic tests confirmed that we could robustly resolve seismic velocity structures to ~20 km depth. In the upper crust (down to ~7 km) beneath central Tenerife, a prominent high-velocity anomaly represents the rigid core of the volcanic complex; at greater depths, a strong low-velocity anomaly reveals abrupt crustal thickening. *Vp* and *Vs* contour lines of 5.2 and 2.85 km/s, respectively, reveal Moho depth variation; crustal thickness beneath Las Cañadas reaches ~17 km, whereas that beneath other parts of Tenerife is ~10 km. An anomaly at ~5 km beneath the caldera with low *Vp*, low *Vs*, and high *Vp/Vs* might be associated with a major phonolitic magma reservoir. Similar anomalies at ~ sea level may represent shallow magma sources responsible for recent eruptions. Seismicity occurs in a columnar area of high *Vp*, high *Vs*, and low *Vp/Vs*, and may represent hydrothermal fluid migration through brittle media. Based on our results, we constructed a conceptual model of volcanic activity on Tenerife.

Plain Language Summary Tenerife is the largest and most populated island of the Canary Islands archipelago. Volcanic activity in Tenerife has the potential to seriously threaten the population and infrastructure. Two main types of volcanism are observed: explosive phonolitic eruptions from the central part of the island and basaltic fissure eruptions along three radial ridges. We present a new seismic tomography model based on the inversion of *P*- and *S*-wave data from local seismicity. Absolute *P*- and *S*-wave velocities reveal abrupt crustal thickening from ~10 to 17 km within an elliptical area coinciding with Las Cañadas caldera in the central part of Tenerife. We suggest a "push-button" mechanism that facilitates vertical displacement of central Tenerife part, which has high topography and is of higher density than peripheral parts of the island. Beneath Teide, at a depth of ~5 km, a low *Vp*, low *Vs*, high *Vp/Vs* anomaly may represent an intermediate phonolitic reservoir. Two similar anomalies at shallower depths may represent the uppermost magma reservoirs directly responsible for phonolitic eruptions. Basaltic eruptions along the three radial ridges appear to be directly fed from mantle sources that appear as high *Vp/Vs* anomalies.

Key Points:

- We constructed a high-resolution seismic velocity model extending to ~20 km depth beneath Tenerife
- The velocity model shows a crustal thickness of up to 17 km below the Las Cañadas caldera and ~10 km below other parts of the island
- The reservoir of phonolitic magma is revealed as an anomaly of low *Vp*, low *Vs*, and high *Vp/Vs* at ~5 km depth

Supporting Information:

Supporting Information may be found in the online version of this article.

Correspondence to:

J. M. Ibáñez,
jibanez@ugr.es

Citation:

Koulakov, I., D'Auria, L., Prudencio, J., Cabrera-Pérez, I., Barrancos, J., Padilla, G. D., et al. (2023). Local earthquake seismic tomography reveals the link between crustal structure and volcanism in Tenerife (Canary Islands). *Journal of Geophysical Research: Solid Earth*, *128*, e2022JB025798. https://doi.org/10.1029/2022JB025798

Received 12 OCT 2022
Accepted 10 MAR 2023

Author Contributions:

Conceptualization: Ivan Koulakov, Luca D'Auria, Janire Prudencio, Jesús M. Ibáñez
Data curation: Luca D'Auria, Iván Cabrera-Pérez, José Barrancos, Germán D. Padilla, Nemesio M. Pérez
Formal analysis: Ivan Koulakov
Funding acquisition: Nemesio M. Pérez
Investigation: Luca D'Auria, Janire Prudencio
Methodology: Ivan Koulakov, Sergei Abramenkov
Resources: Luca D'Auria

1. Introduction

Volcanism in the Canary Islands has the potential to seriously affect the security of population and infrastructure. The recent eruption on La Palma (September–December 2021) did not cause any fatalities, but did destroy hundreds buildings, damaged roads, and seriously disrupted agricultural infrastructure on most parts of the island (Longpré, 2021). Volcanic unrest on El Hierro in 2011–2012 erupted a moderate volume of lava in offshore areas (Carracedo et al., 2012); however, the accompanying strong seismicity caused the evacuation of the island's

Software: Ivan Koulakov
Supervision: Ivan Koulakov, Luca D'Auria, Jesús M. Ibáñez
Validation: Ivan Koulakov, Sergei Abramenkov, Jesús M. Ibáñez
Writing – original draft: Ivan Koulakov, Luca D'Auria, Jesús M. Ibáñez
Writing – review & editing: Janire Prudencio, Iván Cabrera-Pérez

inhabitants. Traces of large calderas on some islands record catastrophic explosive eruptions with the potential to occur again. Some eruptions on the Canary Islands triggered giant landslides that may have produced devastating tsunamis (Paris et al., 2018; Ward & Day, 2001). For this reason, volcanism in the Canaries may also have large-scale impacts on coastal areas around the Atlantic Ocean. Multidisciplinary investigations of magmatic sources and eruptive mechanisms, including better understanding of deep crustal and upper mantle structures, are essential for evaluating the current state of the volcanic system and to forecast its possible future evolution.

In this study, we investigate the deep crustal structure beneath Tenerife, which is the largest (>2,000 km^2) and most populous (~1 million inhabitants) island of the Canary Islands archipelago. Tenerife has a complex geological structure reflecting the long evolution of different volcanic and tectonic processes (Carracedo & Perez-Torrado, 2013; Martí, 2019). Two distinct types of volcanic activity occur on Tenerife (e.g., Ancochea et al., 1990). The first type is dominated by phonolitic magmas originating from shallow crustal reservoirs and causing strong explosive activity (Bryan et al., 1998). These eruptions occur in the central part of Tenerife, within a complex of several merged stratovolcanoes, of which Teide is the central and tallest example. The second type is fissure basaltic eruptions that occur from monogenic vents (e.g., Dóniz et al., 2008). Cinder cones associated with this type of volcanism are found throughout the island (Figure 1), but are mostly concentrated along three major ridges oriented to the northwest, northeast, and south. In historical times (the last 500 years), only eruptions of the second type have been recorded (e.g., Romero, 1992). Although the volumes of lava produced are sufficient to threaten buildings and infrastructure, this type of activity does not pose the same threat to life as the first type.

Owing to its complexity, Tenerife is a focus for scientific investigations in different sub-disciplines of the geosciences. In particular, dozens of papers based on geophysical surveys of Tenerife have been published during the last decade. Gravity modeling results revealed a high-density body located beneath the central part of the island (Araña et al., 2000; Camacho et al., 1991, 2011; Gottsmann et al., 2008). An anomaly of similar shape was identified based on aeromagnetic measurements (Blanco-Montenegro et al., 2011). They concluded that contrasting values of magnetization beneath Teide and Pico Viejo indicate the locations of possible dike intrusions. Magnetotelluric (MT) measurements have been performed on Tenerife for >40 years. The first results by Ortiz et al. (1986) detected strong heterogeneities beneath the Las Cañada caldera, which were interpreted as traces of fluid circulation at relatively shallow depths. Furthermore, they proposed that a conductive layer at ~13 km depth may represent magma underplating beneath the Moho. More details on the crustal structure below Las Cañada were revealed by audio-MT (AMT) studies (Coppo et al., 2008, 2010; Pous et al., 2002). Subsequently, Piña-Varas et al. (2014, 2018) reprocessed the existing data using a novel three-dimensional (3D) algorithm for MT inversion and identified a shallow high-resistivity layer interpreted to be a clay cap overlying deeper low-resistivity areas associated with fluid saturated rocks and shallow phonolitic magma sources.

A series of seismic studies based on active-source data have been performed over the last decade. The first two-dimensional (2D) wide-angle profile shot across the island revealed a high-velocity anomaly beneath the Teide–Pico Viejo volcanic complex (Canales et al., 2000), which was interpreted as a plutonic complex. A large active-source experiment (TOM-TEIDEVS) was carried out by a large international team in January 2007. It included the deployment of 137 seismic stations on the island and air gun shots from an oceanographic vessel that circled the island (Ibáñez et al., 2008). García-Yeguas et al. (2012) performed active source tomography based on these data. The derived 3D distribution of *P*-wave velocity clearly highlights a high-velocity core beneath central Tenerife, which is consistent with the gravity inversion and MT survey results discussed above. Coda waves recorded from active sources in the same station network were used by Prudencio et al. (2015) to evaluate the 3D distribution of *P*-wave attenuation beneath Tenerife. They found that the upper crust down to ~5 km depth is characterized by low-attenuation, whereas the deeper crust is mostly composed of highly attenuated rocks. Data from the TOM-TEIDEVS network were also used for receiver function analysis in Lodge et al. (2012). Although the short recording time did not allow for recording many events, stacking over many temporary stations revealed converted waves of sufficient quality. Beneath Tenerife, they found magmatic underplating and the Moho varying between 15 and 18 km. The same active-source seismic dataset was used by De Barros et al. (2012) to detect zones of scattering by double beam-forming analysis. They identified two levels of high reflectivity, of which the shallow one (1–4 km below sea level [b.s.l.]) corresponded to upper-crustal magma sources and the deeper one (~9 km depth) was interpreted as the Moho interface.

When performing travel time tomography with the use of active source data, robust recovery of anomalies can be achieved down to depths of 5–6 km b.s.l., and is determined by the diving depth of the refracted waves. Thus,

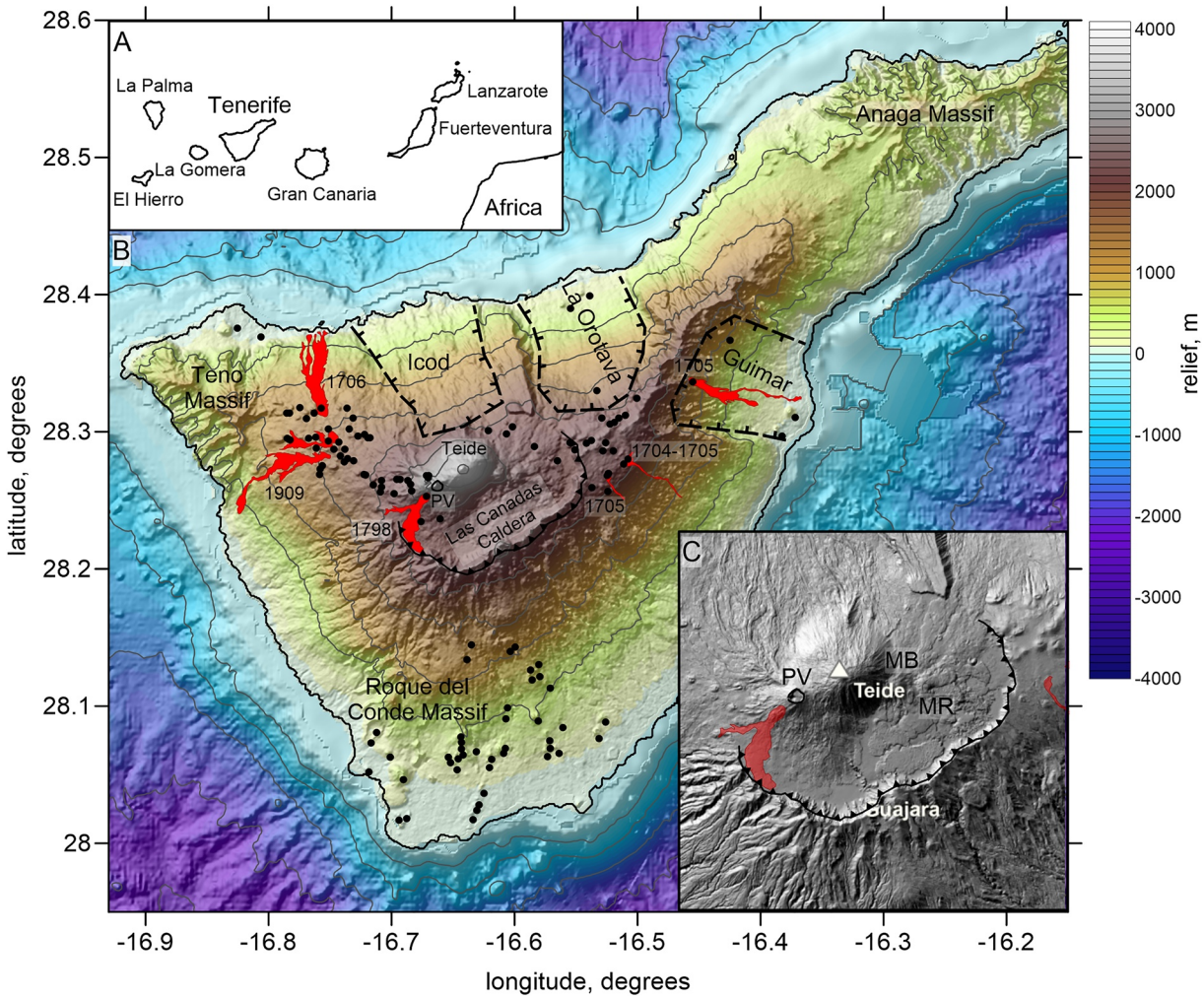

Figure 1. Study area. (a) General view to the Canary Archipelago. (b) Topographic map of Tenerife. The gray contour line highlights the relief with the interval of 500 m. The dashed lines with ticks mark the locations of the large landslides. The red areas depict the lava flows of historical eruptions with indicated years. The black dots highlight the clearest cinder cones. (c) The detailed map of the Las Cañadas Caldera and Central Volcanic Complex. Abbreviations: PV, Pico Viejo; MB, Montaña Blanca; MR, Monte Rajada.

García-Yeguas et al. (2012) could not provide any information on mantle structures, which are essential to understanding deep magma sources. Furthermore, the active-source survey could only provide *P*-wave data. As shown by many seismic studies of volcanoes (e.g., Bushenkova et al., 2019; Koulakov et al., 2021; Vargas et al., 2017), joint interpretation of *P*- and *S*-wave velocities can give much richer information to interpret tomography results in terms of melt and fluid distributions.

In this study, for the first time for Tenerife, we performed the inversion of *P*- and *S*-wave arrival times from local seismicity that occurred beneath the island. Although a large number of different geophysical studies have previously been conducted on this island, our results offer important new insight to into the processes of magma feeding in the crust and uppermost mantle beneath Tenerife. Moreover, we compared our results with 3D seismic models of La Palma and El Hierro, derived previously using the same algorithm, in order to highlight commonalities and differences in the construction of islands in the archipelago.

2. Tenerife Island

Tenerife is the largest island of the Canary Islands archipelago, which is located in Atlantic Ocean at a distance of 320 km from the African coast. Tenerife Island formed as a result of a long series of volcanic and tectonic episodes. The initial origin of volcanism in this part of the Atlantic remains a subject of debate, with hypotheses

including a mantle plume (e.g., Canas et al., 1998) or asthenospheric upwelling due to mechanical flexure of the Atlantic lithosphere on the margin of the African Plate (i.e., Anguita & Hernán, 2000). Regardless, the formation of Tenerife began at >20 Ma with the growth of a large submarine shield volcano to a diameter of approximately 100 km (Carracedo & Perez-Torrado, 2013). The first sub-areal structures appeared as three separate islands between 12 and 3.3 Ma as a result of basaltic fissure eruptions (Ancochea et al., 1990); their remnants, known as the Teno, Anaga, and Roque del Conde massifs, are located at the northwestern, northeastern, and southern edges of the island, respectively. At ∼3 Ma, these structures became interconnected owing to intense eruption activity in fissure zones, giving birth to three ridges of NW–SE, NE–SW, and S–N orientations. High eruption activity at the triple junction of these ridges in the central part of the island resulted in the formation of the pre-Cañadas structure, which was the highest part of the island and reached an altitude of ∼2,500 m (Carracedo & Troll, 2013). Constructive activity coexisted with destructive processes, some of which were catastrophic (Hurlimann et al., 1999). For example, two giant landslides occurred at approximately 800 ka, forming the valleys of La Orotava and Güímar.

The large Las Cañadas caldera, which extends 16 × 9 km across the central part of the island, formed at approximately 200 ka (Martí, 2019). The origin of the caldera appears to be connected with a large northward-directed landslide in the Icod Valley. The relative timings of the processes that caused the formation of these two structures remain a subject of debate (Martí, 2019). Some authors argue that the caldera-shaped structure was not of volcanic nature, and was formed by a landslide caused by gravitational instability, similar to La Orotava and Güímar (Ancochea et al., 1999; Cantagrel et al., 1999). Others have suggested that a large caldera-forming eruption of felsic magma caused the vertical collapse (or a series of successive collapses) within the caldera and triggered the landslide (Brown & Branney, 2004; Bryan et al., 1998; Martí et al., 1997; Martí & Gudmundsson, 2000). The latter concept is supported by the presence of Plinian pumice and ignimbrite deposits corresponding to this time (Booth, 1973; Brown & Branney, 2004).

Today, the southern border of the Las Cañadas caldera forms a 500 m high cliff that creates an amphitheater surrounding the Central Volcanic Complex, which includes a group of merged volcanic edifices (Pico Viejo, Pico del Teide, Montaña Blanca, and Monte Rajada). The Teide stratovolcano, which is located in the central part of this inter-caldera complex at the intersection of two fissure zones, was constructed during the last 175 ka by a series of phonolitic and basaltic trachibasaltic eruptions (Ablay & Martí, 2000). Teide currently has an altitude of 3,715 m and it is considered among the volcanoes with the highest relative elevations in the world.

In summary, two extreme types of volcanic processes formed Tenerife: effusive basaltic flows along a series of fissures and explosive eruptions of phonolitic lavas that occurred mostly in the central part of the island. The fissure basaltic volcanism is fed by deep magma sources, presumably located below the Moho, whereas phonolitic magmas are fed from a series of shallow reservoirs (Bryan et al., 1998; Edgar et al., 2007; Martí & Gudmundsson, 2000; Mitjavila & Villa, 1993; Wolff et al., 2000). According to petrological studies, the Teide and Pico Viejo feeding reservoirs are located at depths of 4–5 km below surface, whereas storage for Montaña Blanca and Roques Blancos is at ∼1–2 km below surface (Andújar & Scaillet, 2012; Andujar et al., 2013).

Recent volcanic activity appears to be extremely diverse and includes lava flows ranging from basalts to phonolitic lavas, eruptions from large stratovolcanoes, monogenic cones, and calderas, and massive pyroclastic flows. Most basaltic flows are associated with fissures oriented along the three extensional structures that form the triple junction and determine the triangular shape of the island (Carracedo & Troll, 2013). The most prominent of the lineaments are the NE–SW-oriented Dorsal Ridge and NW–SE-oriented Santiago del Teide Ridge.

Well-expressed cinder cones representing the locations of monogenic basaltic eruptions are highlighted in Figure 1. The maximum age of these cones is ∼800 ka; however, most are younger than 170 ka and formed in the post-caldera period (Ancochea et al., 1990). Inside the caldera, monogenic cones are less common. The estimated recurrence time of such monogenic eruptions is relatively small (Dóniz et al., 2008); as >100 years has passed since the most recent eruption, a new eruption is plausible in the near future.

The Global Volcanism Program database provides the characteristics and dates for dozens of eruptions on Tenerife within the last 7,000 years (Global Volcanism Program, 2013). In recent geological history, the strongest eruption, a Volcano Explosivity Index (VEI)-4 event, occurred on Montaña Blanca and Pico Viejo 2,000 years ago, as determined by radiocarbon analysis (Ablay et al., 1995). In historical times, five eruptions with lava flows have been recorded (Romero, 1992). The first was a 1,492 eruption at Garpaccio on the NE–SW-oriented Dorsal

Ridge. Between 1704 and 1706 a sequence of VEI-2 eruptions occurred along the NE Ridge (Siete Fuentes, Fasnia, Güímar) and NW Ridge (Garpachio); one of the lava flows in this sequence destroyed the city and port of Garachico. The largest historical eruption, a VEI-3 event, occurred on the SW flank of Pico Viejo in June–September 1798. Finally, the most recent magmatic eruption, a VEI-2 event, occurred in 1909 from the El Chinyero vent on the NW Ridge.

The Teide crater exhibits continuing fumarole activity. The composition is dominated by water vapor and CO_2, but also contains gases such as N_2, CH_4, H_2, He, O_2, Ar, He, H_2S, SO_2, and CO (Albert-Beltran et al., 1990; Melian et al., 2012). There is evidence for both meteoric and magmatic water in fumarolic gasses (Albert-Beltran et al., 1990; Melian et al., 2012). Dispersed hydrothermal activity is also observed in other parts of the Las Cañadas caldera, such as that around Montaña Blanca (Perez et al., 2013). Carracedo et al. (2007) attributed this activity to the circulation of fluids around a shallow magma reservoir that has fed recent eruptions of Montaña Blanca.

Ongoing seismic monitoring by a network of permanent stations shows generally low background seismic activity. In quiet periods, no more than 10 events per month occur, with most tectonic in nature, occurring offshore between Tenerife and Gran Canaria at a distance of 70–100 from the Tenerife coast. However, in recent years, several seismic swarms beneath the island have plausibly been linked to magmatic activity. In April–May 2004, >200 notable events with magnitudes of 1–3 were recorded (Almendros et al., 2007). Seismic activity beneath the island remained higher than average throughout 2005. Another seismic swarm began in October 2016, when at least 700 discrete events were recorded (D'Auria et al., 2019). Most were located at depths of ∼8 km b.s.l. beneath the southern rim of Las Cañadas caldera. The increased seismicity continued after 2017, but shifted to the area beneath Teide. These swarms were interpreted as a result of magmatic fluid injection into the hydrothermal system; however, they were not accompanied by any significant ground deformations (D'Auria et al., 2019). These swarms triggered an increase in degassing from the Teide cone; from before 2004 to after 2017, CO_2 emissions increased from 50 to 354 tons per day, while H_2S rose from 35 to 152 tons per day (Padrón et al., 2021). Moreover, remarkable changes in groundwater chemistry were observed (Amonte et al., 2021, 2022). Although these episodes of unrest did not lead to magmatic eruptions, they confirmed that the magma plumbing system remains active. In this study, we used local earthquake data recorded during these seismic swarms to perform passive-source tomography.

3. Data and Algorithms

On Tenerife, there are two seismological networks, those operated by the Instituto Volcanológico de Canarias (INVOLCAN; 21 stations) and Instituto Geográfico Nacional (IGN; 19 stations). In this study, we used IGN data from 28 January 2001–14 November 2021, and INVOLCAN data from 30 November 2016–12 November 2021 (Figure 2). While operating simultaneously, these two agencies independently provided source solutions based on their own stations. Initially, the IGN dataset contained 8,985 events with 57,762 *P*- and 77,292 *S*-wave picks; the INVOLCAN catalog contained 7,898 events with 27,619 *P*-and 49,496 *S*-wave picks. In our study, we merged these data. The origin times and coordinates of the same events in IGN and INVOLCAN are slightly different because they use different velocity models and algorithms for source locations. Therefore, when merging the data, for an event in one dataset we searched for any event in the second dataset with a difference in origin time of <1 s. Then, we compared their locations and considered them as a single event if the difference in locations was <10 km. Using this method, we could not exclude cases of wrong merging, when we identified two separate events as one. In this case, at the step of source relocation within the tomography workflow, we had too large residuals for such events, which were rejected. In any case, the number of such events occurring almost simultaneously is low, and in case of their misinterpretation, they do not affect the final tomography model. After merging the data, we identified 5,073 common events, 2,825 non-paired events in the IGN catalog and 3,933 non-paired events in the INVOLCAN catalog. As such, the final merged catalog contained 11,831 events with 85,566 *P*- and 127,037 *S*-wave picks. The mean number of picks per event was 17.97. The larger number of the S-wave picks is caused by significantly higher amplitudes of the *S*-wave arrivals, which in some cases are better recognizable above the noise level than the *P*-wave arrivals. An example of a typical seismogram showing clearer *S*-wave phases is presented in Figure S1 in Supporting Information S1.

The distributions of the event magnitudes versus the observation time are plotted in Figure S2 in Supporting Information S1. For magnitudes, we used primarily the solutions of INVOLCAN if they were available; otherwise, we took the IGN determinations. It can be seen that after November 2016, the number of events considerably

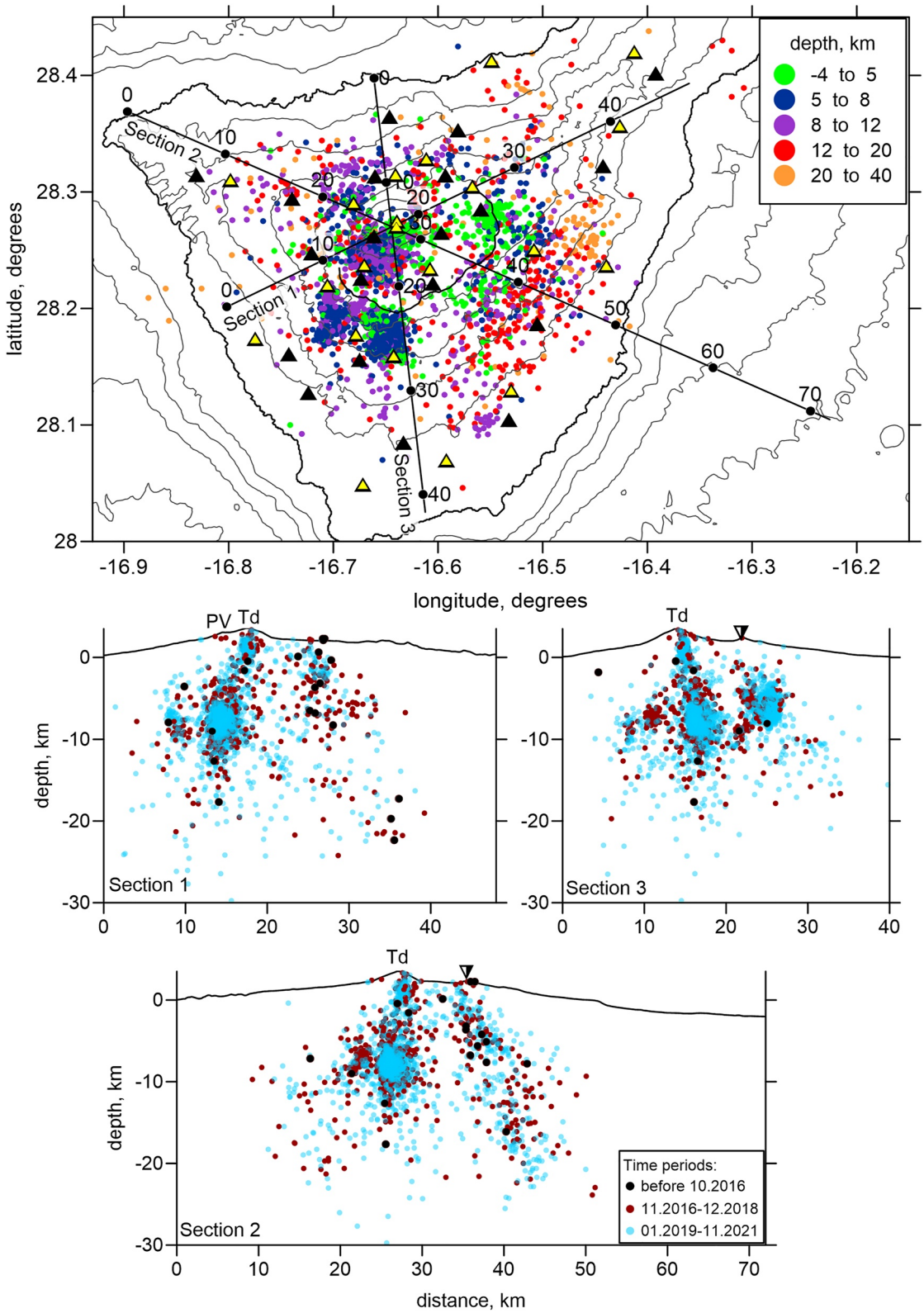

Figure 2. The final distributions of seismicity used in this study in map view and projected in three vertical sections. In the map, the colors of dots indicate the depth intervals according to the scale. The black and yellow triangles depict the seismic stations of INVOLCAN and IGN, respectively. The contour lines mark the relief with the interval of 500 m. In the vertical sections, the events at the distances of less than 5 km from the profile are shown. The inverted triangle marks the border of the caldera. Abbreviations: Td, Teide; PV, Pico Viejo.

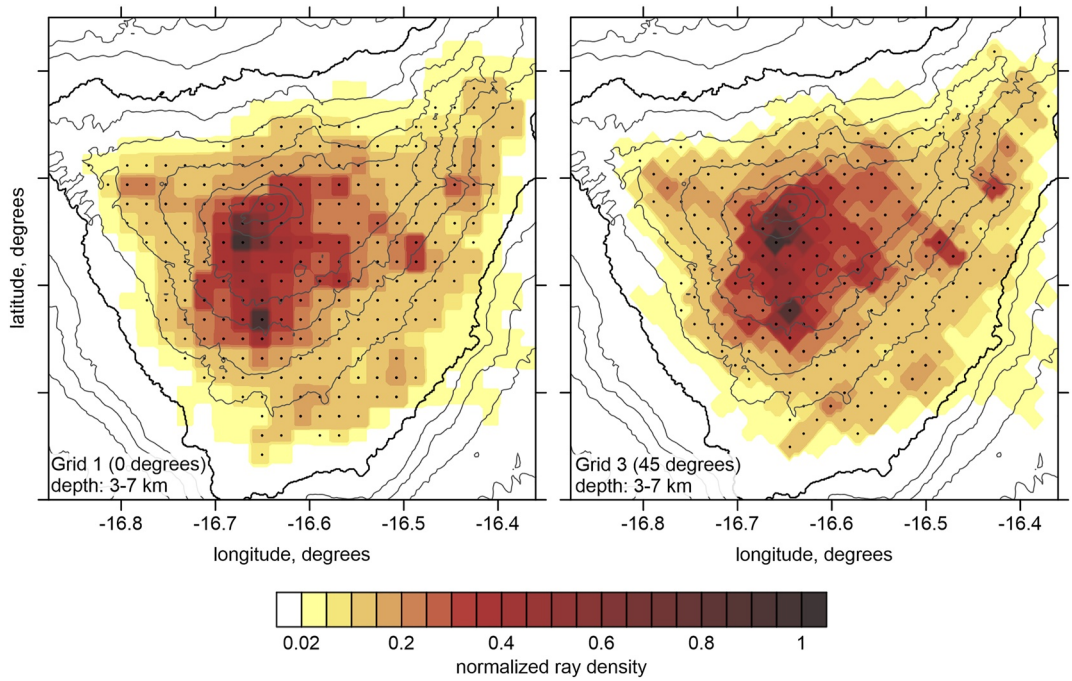

Figure 3. Distributions of the ray density and nodes in the depth interval of 3–7 km for two grids with different basic orientations. The contour lines mark the relief with the interval of 500 m.

increased due to the deployment of the INVOLCAN seismic network that improved the sensitivity of the seismicity identification. For the whole period, the magnitudes of the events ranged between 1 and 2.5; however, after 2017, a large number of events below the magnitude 1 were detected. The strongest events with the magnitudes of 4 and higher occur approximately one time per 2 years.

For tomography, we selected events with a total number of *P*- and *S*-wave picks of ≥8. The time residual absolute values for locations in the starting one-dimensional (1D) model should not be larger than 0.7 s. If an event was located >20 km from the nearest station, it was removed from consideration. This criterion has moved out numerous tectonic events located offshore between Tenerife and Gran Canaria at distances of ∼70–100 km from the Tenerife shore. After these selection criteria, the dataset used for the tomography was reduced to 6,731 events with 53,974 *P*- and 78,969 *S*-wave picks.

The tomographic inversion was performed using the LOTOS code for passive-source body-wave tomography (Koulakov, 2009). This code has been implemented in a large number of studies and is particularly suitable for studying volcanoes (e.g., Bushenkova et al., 2019; García-Yeguas et al., 2014; Koulakov et al., 2020, 2021). One of the most recent examples is La Palma, another island of the Canary Islands archipelago, for which the tomography model inferred the structure of the magma source during an ongoing eruption in 2021 (D'Auria et al., 2022).

The algorithm is described in detail by Koulakov (2009) and Koulakov et al. (2020, 2021); here, we briefly highlight the major features and present the parameter values used in this study. The processing workflow starts from the preliminary source location, which uses a 1D velocity model and grid-search method to determine the optimal coordinates of events. For this stage, we used a simplified method of travel time calculation based on the straight paths of the rays. Subsequently, we used another source relocation algorithm in the 3D velocity model based on the gradient method of optimization and the bending ray tracing algorithm.

The velocity model was parameterized using a set of nodes distributed in the study volume according to the density of rays, as shown in Figure 3. In map view, they were distributed regularly with a constant step of 2 km, but placed only in areas with sufficient ray coverage (>0.1 average ray density). In the vertical direction, grid spacing was inversely dependent on the ray density, but could not be <1 km. To minimize the effect of grid geometry on the resulting velocity model, we performed several inversions in grids with different basic azimuthal orientations (0, 22, 45, and 66°) and then averaged the results in one regularly spaced model. Examples of two grids

Table 1
Major Controlling Parameters Used for Calculation of the Main Tomographic Model

Parameter	Value
Smoothing for the *P*-wave velocity	0.7
Smoothing for the *S*-wave velocity	2.0
Amplitude damping for the *P*-wave velocity	0.3
Amplitude damping for the *S*-wave velocity	0.7
Weight for the station corrections	0.5
Weight for corrections of source coordinates	0.5
Weight for corrections of source origin times	0.5

with the orientations of 0 and 45° are shown in Figure 3. The distribution of nodes determines the shape of the visualized area when presenting the results of tomographic inversion. The derived velocity parameters are presented in areas where the distance to the nearest node is less than 4 km. The areas without nodes, where the ray coverage insufficient, remain blank. The inversion was performed simultaneously for the 3D distributions of the *P*- and *S*-wave velocity anomalies, station corrections, source coordinates, and origin times. The stability of the inversion was controlled by amplitude damping and flattening regularization. The inversion of the large sparse matrix was performed using Least Squares with QR decomposition (LSQR; Nolet, 1987; Paige & Saunders, 1982). All controlling parameters used for inversion are presented in Table 1. The optimal values of these parameters were assessed based on the results of synthetic modeling, which are described in Section 4.

In some tomography studies, to assess the values of damping parameters, the authors use so called trade-off curves (TOC) or L-shaped curves, which represent the dependency of the data variance versus model variance for different values of damping (Eberhart-Phillips, 1993). It is presumed that the corner area of such a curve indicates the optimal values of damping coefficients. However, we find this method not sufficiently grounded and never use it in our studies. As shown by Koulakov (2009, 2020), in this approach, there are several obvious flaws that may bring to erroneous solutions. Nevertheless, following the reviewer's persistent demands, we have constructed the TOCs for the amplitude damping and smoothing and calculate the velocity models for the experimental and synthetic data using the derived parameters. The results of these exercises are presented in Supporting Information S1 (Figures S3 to S6). The main conclusion is that the TOC-based inversion parameters give too low amplitudes of anomalies, especially the P-wave velocity model. Therefore, we insist that our approach based of synthetic modeling gives more appropriate values of damping parameters.

After creating a new 3D velocity model, we returned to the next iteration, which included source relocation in the updated 3D model, a new matrix calculation, and inversion. In total, we performed five iterations. The values of the average residuals and variance reductions during iterations (*dtp*) in L1 norm are presented in Table 2.

The 1D starting velocity model was defined by running the complete tomographic procedure several times. In each run, we defined the *P*-wave velocity model based on the average velocity values in horizontal slices at several depths determined in the previous run. Between these depth levels, the 1D velocity was linearly interpolated. After several successive runs, we achieved an approximate balance of positive and negative anomalies of *P*-wave velocities at each depth. At the same time, in the staring models, we always defined a constant *Vp/Vs* ratio to avoid any predefinition of this parameter. Therefore, the *S*-wave velocity anomalies were not always balanced. The values of the *P*-wave velocities in the final model used to calculate the main result are shown in Table 3. In this case, the *Vp/Vs* ratio in the starting model was equal to 1.83.

Note that this method is different from that used by some other authors who construct the reference velocity model based on the minimization of the residuals (Kissling et al., 1994). This approach may give strongly biased results due to inhomogeneity of data distributions as illustrated in Figure S7 in Supporting Information S1. For example, if ray paths are densely concentrated within a low-velocity zone, residual minimization will cause a general reference velocity decrease. At the same time, we found that the resulting velocity variations remain stable in a broad range of the reverence velocities. For example, in Figure S8 in Supporting Information S1, we show an example of the model inversion with an increased reference velocity with values higher than in the main model to 1 km/s. It can be seen that despite such a considerable change of the reference velocity model, the main patterns of the velocity variations remain stable. This problem is further discussed in Supplementary.

Table 2
Mean Residuals in L1 Norm and Their Variance Reductions During the Iterative Inversion Procedure

Iteration	Mean dtp, s	Reduction dtp, %	Mean dts, s	Reduction dts, %
1	0.241	0	0.279	0
2	0.142	41.0	0.195	30.0
3	0.135	43.9	0.184	34.0
4	0.132	44.9	0.181	35.2
5	0.131	45.5	0.179	35.9

Table 3
P-Wave Velocities in the Starting Model

Depth, km	*Vp*, km/s
−5	3.8
0.5	4.2
5	4.45
10	5.17
15	5.5
20	6.0
30	7.4

Note. The *S*-wave velocity in the starting model was calculated using the constant $Vp/Vs = 1.83$.

4. Synthetic Tests

We used synthetic tests to assess the spatial resolution of the model. For this, we aimed to closely simulate the conditions of the experimental data processing. To define the rays for the modeling, we used the same source–receiver pairs as in the experimental dataset; the locations of the events were taken from the final solution derived in the main model. The synthetic model was defined by a set of 3D anomalies overlapped to the reference 1D model. The synthetic travel times were calculated in the 3D model by the bending algorithm of ray tracing. The obtained travel times were perturbed by random noise having a predefined average deviation, in our case, 0.1 and 0.2 for the *P*- and *S*-wave data, respectively. The noise has the non-Gaussian statistical distribution with the histogram shape taken from real seismological datasets. These levels of noise were chosen to achieve approximately the same variance reduction as in the case of experimental data inversion. It was important that after computing the synthetic travel times, we "forgot" the true locations of the sources and origin times, and repeated the same stages of the tomographic procedure as in the case of experimental data. The number of iterations and all controlling parameters during synthetic model recovery were the same as those used in when computing the main model. In these synthetic tests, we tuned the values of controlling parameters to obtain the best recovery quality; we then used these optimal values for the inversion of experimental data in the main model. In this sense, the synthetic modeling and inversion of experimental data were conducted concurrently.

In Figure 4, we present the result of the checkerboard test, in which the synthetic anomalies are represented by cubes of 5 × 5 × 5 km size separated by empty intervals of 2 km width. Inside these cubes, we defined alternated anomalies with amplitudes of ±8%. For *dVp* and *dVs*, the signs of the anomalies were opposite to enable high contrasts of the *Vp/Vs* ratio. With added noise of 0.1 and 0.2 s for the P and S wave data. After five iterations, the inversion provided variance reductions of ∼30% and ∼26% for the *P*- and *S*-wave data, respectively, which are similar, or even smaller than those of the experimental data inversion (see Table 2). The recovery results in Figure 4 are shown in three depth sections roughly corresponding to the central parts of the anomalies in separate layers. It can be seen that at a depth of 1 km, the derived anomalies have slightly higher amplitudes (10%–11% instead of the original 8%); in the second layer at 7 km depth, the amplitudes appear to be close to the original values and in the deepest layer at 14 km, the anomalies are much weaker. It is obvious that one set of damping parameters cannot enable ideal recovery of amplitudes in all parts of the study volume. If for example, we request the correct recovery of amplitudes in the shallow section and increase the damping, we can lose some amplitude in deeper sections, and some relevant anomalies may disappear. Therefore, when selecting the damping value, the main requirement was the stability of shapes of the anomalies and absence of artifacts caused by noise. For the amplitudes, we keep in mind the general patterns observed in the synthetic tests and then take them into account when interpreting the results of experimental data inversion.

Vertical resolution was further tested using another series of tests (Figure 5), in which the anomalies were defined in the same profiles as used for presenting the main results. In the plane of the profile, synthetic alternated anomalies with amplitudes of ±8% were defined in squared cells of 5 km size separated by 2 km of empty space. Across the section, anomalies were 8 km in size. For each of the three sections, we performed three independent tests. The level of noise was the same as that for the checkerboard tests (0.1 and 0.2 s for *P*- and *S*-wave data, respectively). For most cases, the inversion enabled robust recovery of anomalies in the upper two rows (<10 km depth). In the third row, anomalies were still visible, but appeared to be smeared. This fact should be taken into account when interpreting the main model.

In the final test shown in Figure 6, we have designed a synthetic model with realistic structures. The anomalies were defined inside free-shaped polygons in the vertical Section 2, same as used for presenting the main results. The thickness of the anomalies in the direction across the section was 8 km. The shapes of the original structures and values of the anomalies are presented in the upper row of Figure 6. The recovery results are given in relative anomalies (middle row) and absolute velocities (lower row). It can be seem that the inversion reconstructs all the main patterns defined in the model that also exist in the main model resulted from the inversion of experimen-

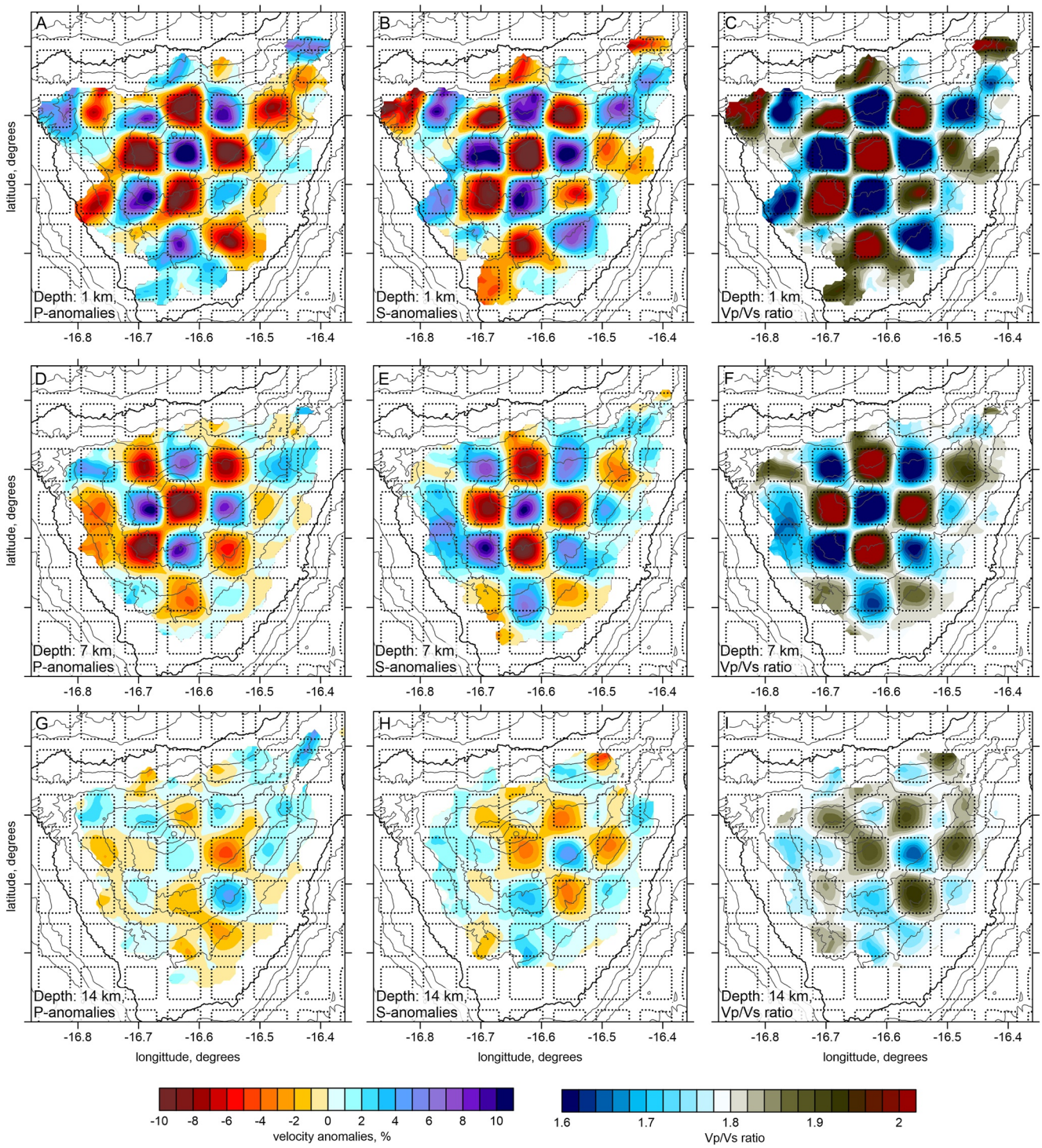

Figure 4. Checkerboard test to assess the spatial resolution. The anomalies are defined in cubes of 5 × 5 × 5 km separated by empty interval of 2 km. The recovered results for the dVp, dVs, and Vp/Vs ratio are shown in three horizontal sections. The shapes of the synthetic anomalies are highlighted with the dotted lines. The gray contour lines indicate the relief with the interval of 500 m.

tal data. In particular, it is important that with our data we can resolve a strong flexure in absolute velocities at large depth highlighted with dotted line. In the main model, a similar structure is interpreted as an abrupt Moho deviation. It is also important that we can resolve a "magma chamber' – a low-velocity anomaly below Teide at ~5 km depth.

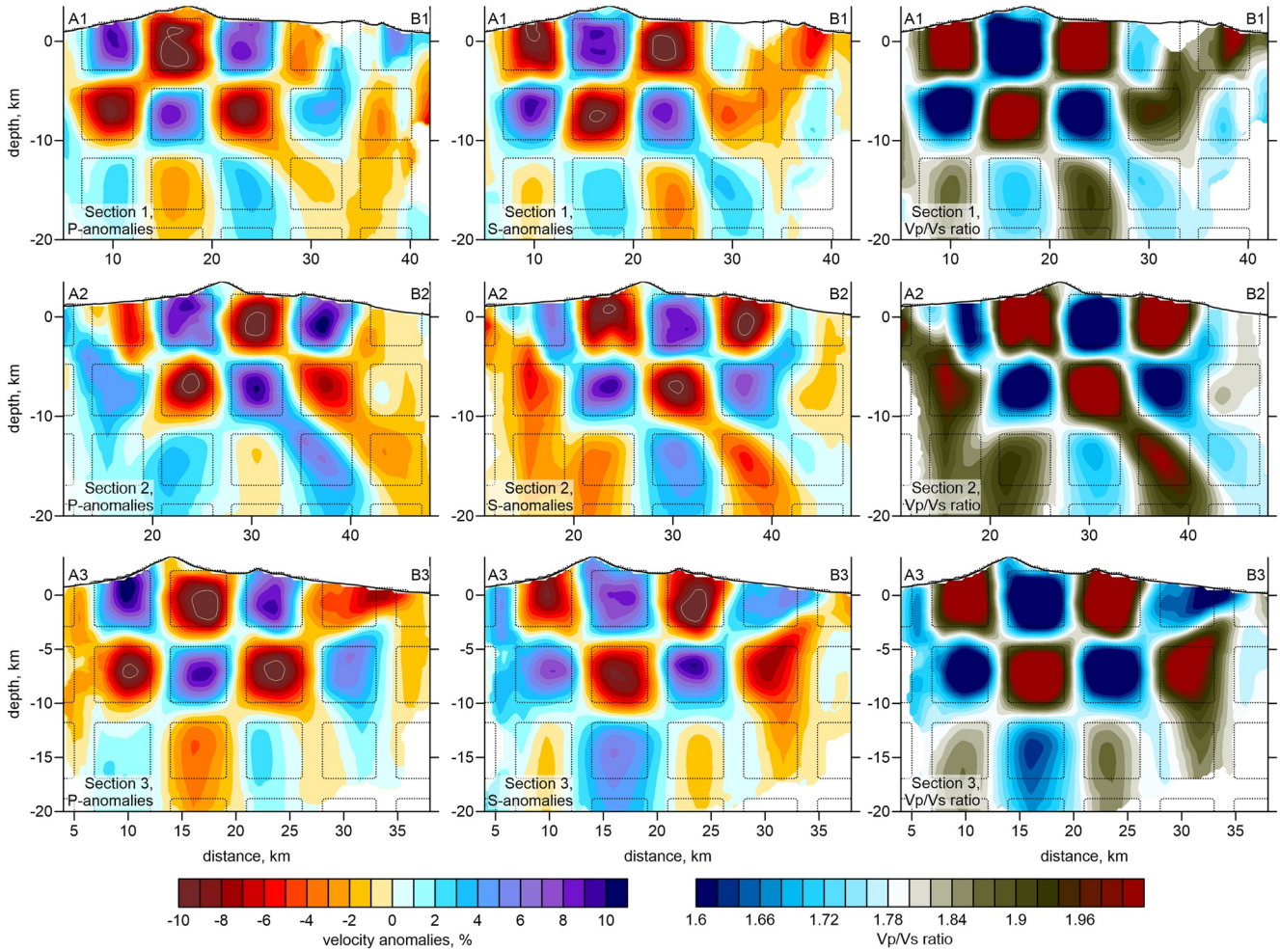

Figure 5. Results of three checkerboard tests for the P and S wave anomalies and Vp/Vs ratio defined in three vertical sections, same as used for presenting the main results in Figure 9. Dotted lines indicate the shape of the synthetic anomalies.

Besides the tests discussed above, we have performed a series of spike tests, in which a small single anomaly is defined in selected points of the study area. In Figure S9 in Supporting Information S1, we present an example of such a test with a spike having the size of $4 \times 4 \times 4$ km located in the central part of the area. It can be seen that this anomaly is recovered almost without smearing. For anomalies located below 10 km depth of at the periphery of the study area, the reconstruction quality was much poorer. The same features are seen in the result of the checkerboard test in Figure 4, that is why we do not present the spike tests in the main paper.

As discussed, after computing the synthetic times, we "forgot" the true locations of the sources; as such, this test allowed us to estimate realistic event mislocations. Figure 7 shows event solutions for the model with realistic anomalies presented in Figure 6. Here we show the initial locations in the 1D model using the grid-search model and the locations in the final recovered model. In the preliminary locations in the 1D velocity model, the average bias of the coordinates was 1.38 km. In the final model, after five iterations of inversion and relocation, the average source location error was reduced to 0.71 km. Despite the remaining mislocations, the main anomalies in this test were correctly recovered in most parts of the study area (Figure 6).

5. Tenerife Island Tomography

In Figure 2 we present the distributions of seismic events determined simultaneously with the 3D velocity model. As demonstrated in Figure 7 for the case of synthetic model, the use of the 3D velocity model gives much more accurate solutions compared to the standard determinations in the 1D reference models provided by INVOLCAN and IGN. In our result, we observe more concentrated clusters better highlighting the existing volcanic and

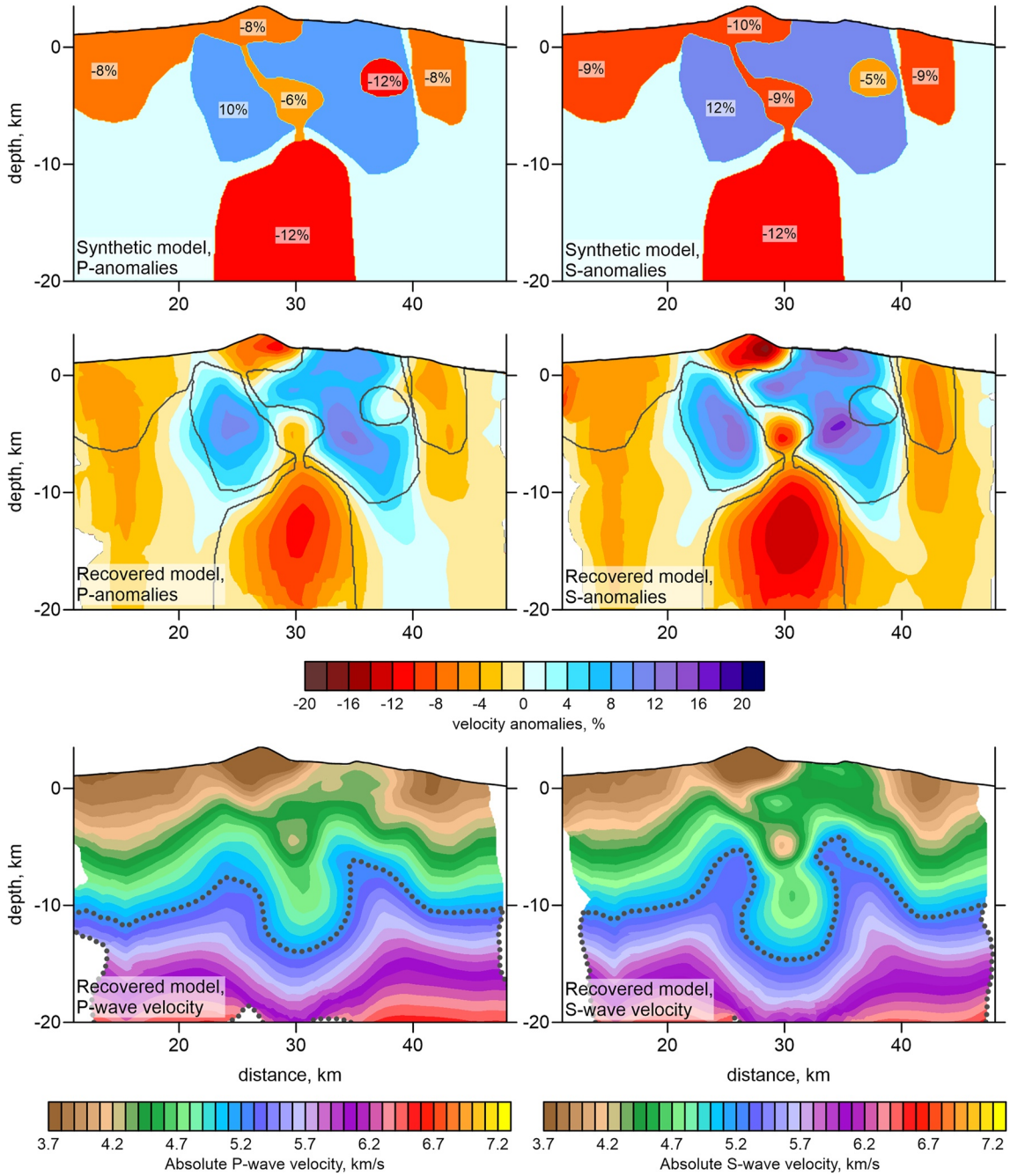

Figure 6. Synthetic test with realistic shapes of anomalies in Section 2, same as used for presenting the main results in Figure 9. Upper row presents the initial synthetic models for the P and S wave velocity anomalies. The values of anomalies are indicates with numbers. Middle row shows the recovered anomalies, and the lower row is the absolute velocity distributions. In the middle row, the shapes of the initial anomalies are highlighted with contours. In the lower row, the dotted line represents the velocity levels of 5.2 km/s and 2.85 km/s for the P and S wave velocities, respectively.

tectonic structures compared to the previous solutions. It should be noted that our source locations are closer to the INVOLCAN determinations, which shows that they are using a more appropriate velocity model. For the future, we encourage both institutions to use our 3D velocity model and our location algorithms for routine locations of seismicity beneath Tenerife.

From our tomographic inversion, we obtained the 3D distributions of *P* and *S*-wave velocities, as well as the coordinates of events relocated in the final velocity model. Figure 8 shows the *Vp* and *Vs* anomalies in four horizontal sections from 0.5 to 15 km (b.s.l.). Figure 9 shows the *Vp* and *Vs* anomalies in three vertical sections. Figure 10

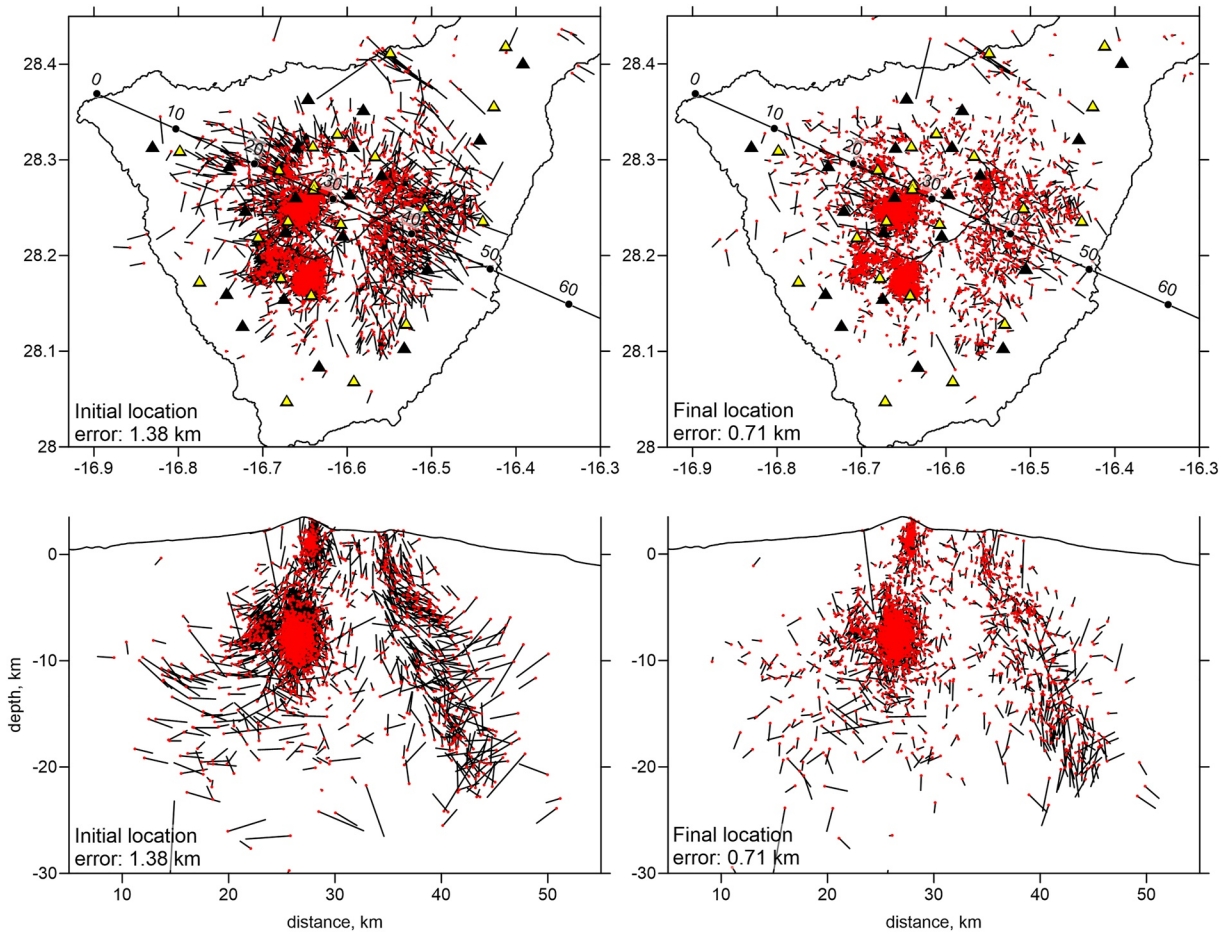

Figure 7. Source mislocations in map view (upper) and vertical section (lower) corresponding to the synthetic test with realistic anomalies shown in Figure 6. The red dots are the current source locations, and the black bars indicate to the true locations. Preliminary source locations after grid search in the 1D starting models are in the left column. The right column present the results of source locations in the final 3D model. The average mislocation values are indicated in each panel.

shows the absolute values of *Vp* and *Vs*, and the distribution of *Vp/Vs* ratios. The *Vp/Vs* ratio was computed by simple division of the derived absolute velocities of *Vp* over *Vs*. The suitability of this method was confirmed by the synthetic modeling results (Figures 4 and 5). The final locations of the events are shown in the same vertical sections (Figures 9 and 10), and in Figure 2.

In Figure 8, two shallow depth sections of both *P*- and *S*-wave velocity models reveal a distinct high-velocity core located beneath the central part of the island; this core is surrounded by low-velocity anomalies. This feature is generally consistent with a prominent high-velocity anomaly in a previous seismic velocity model based on active source data (García-Yeguas et al., 2012), as well as with a large, central low-attenuation body in an attenuation tomography model (Prudencio et al., 2013). Moreover, a similar body with high density was detected in gravity field modeling (Camacho et al., 2011) and in MT analysis (Piña-Varas et al., 2018). However, our data also reveal a new feature, a local low-velocity anomaly beneath the southeastern flank of Teide at a depth of 5 km; this feature is consistent in both the *P*- and *S*-wave models.

Anomalies in the deeper sections differ considerably from the shallower structures. Both *P*- and *S*-wave models show a highly-contrasted low-velocity anomaly roughly coinciding with the caldera contour. A similar transition of seismic properties was identified in the attenuation tomography model of Prudencio et al. (2015), in which attenuation was low above 5 km b.s.l. and high in deeper sections.

We interpreted our results in terms of crustal structures and magma sources based on the obtained seismic attributes including the absolute velocities, velocity anomalies and *Vp/Vs* ratio. Based on the different seismic parameters in the *P*- and *S*-wave sections, Figures 11 and 12 show the main major structural elements identified.

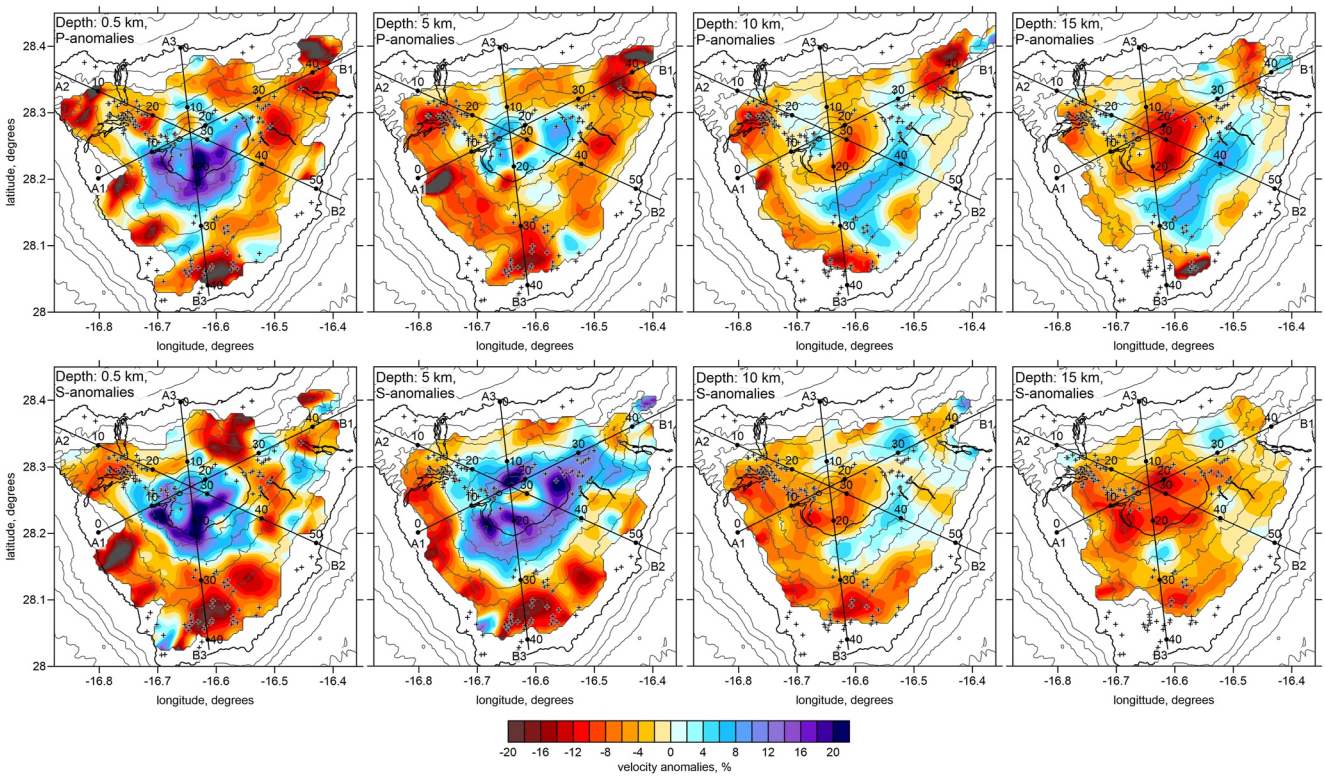

Figure 8. Results of the experimental data inversion in four horizontal sections. The gray contour line highlight the relief with the interval of 500 m. The lava flows of historical eruptions are highlighted with the thin contours. The crosses highlight the clearest cinder cones. The locations of the three vertical sections are shown.

A conceptual model constructed with the use of our results is presented in Figure 13. Our new tomography model reveals new information about the shape of the Moho beneath Tenerife. In general, seismic tomography is concerned with continuous velocities and does not include first-order interfaces with sharp changes in velocity. However, as noted in several studies (Di Stefano et al., 2009; Khrepy et al., 2016; Koulakov et al., 2015), in some cases, the geometry of contour lines in continuous velocity models can indicate variation of a first-order interface, such as the Moho. For example, crustal thinning is associated with high-velocities and upward undulations of contour lines in tomography models. In contrast, thicker crust is normally shown as a low-velocity anomaly with downward displacement of the corresponding velocity contour lines.

The coexistence of shallow high velocity and deeper low-velocity beneath the central part of Tenerife results at almost no increase in absolute *P*- and *S*-wave velocities down to a depth of 15–17 km (see absolute velocities in Figure 10). We suggest that the contour lines of absolute *P*- and *S*-wave velocities at 5.2 and 2.85 km/s, respectively (see dotted lines in Figure 10), represent the Moho interface. Differences in the shapes of these contours could reflect the different sensitivities of *P*- and *S*-wave velocities to other petrophysical parameters, such as composition, temperature, and fluid content. Based on joint consideration of these contour lines, we constructed a possible shape of the Moho interface along vertical Sections 2 and 3 (bold solid lines in Figures 11 and 12). Beneath marginal parts of Tenerife, these contour lines are located at depths of 10–12 km b.s.l. In contrast, beneath the central part of the island they abruptly deepen to 16–18 km b.s.l.; that is, the Moho depth beneath central Tenerife is up to 7–8 km deeper than that in surrounding areas. In map view, the low-velocity anomaly causing such strong deepening of the Moho almost perfectly coincides with the limits of the Las Cañadas caldera. Thus, the flexure on the Moho interface appears to be roughly isometric with a diameter of ∼10 km, which is comparable with the value of the Moho deepening.

This area of local crustal thickening corresponds to the very high topographical feature of Teide volcano (altitude of 3,715 m above sea level). At the same time, this area is characterized by a high-density anomaly, as revealed by gravity modeling (e.g., Gottsmann et al., 2008). Both of these factors create excessive weight in the crust, which has to be isostatically compensated for by crustal thickening. The width of Moho flexure due to the isostatic mechanism is limited by the strength of the crust. For developed continental crust of 40–50 km thick, such

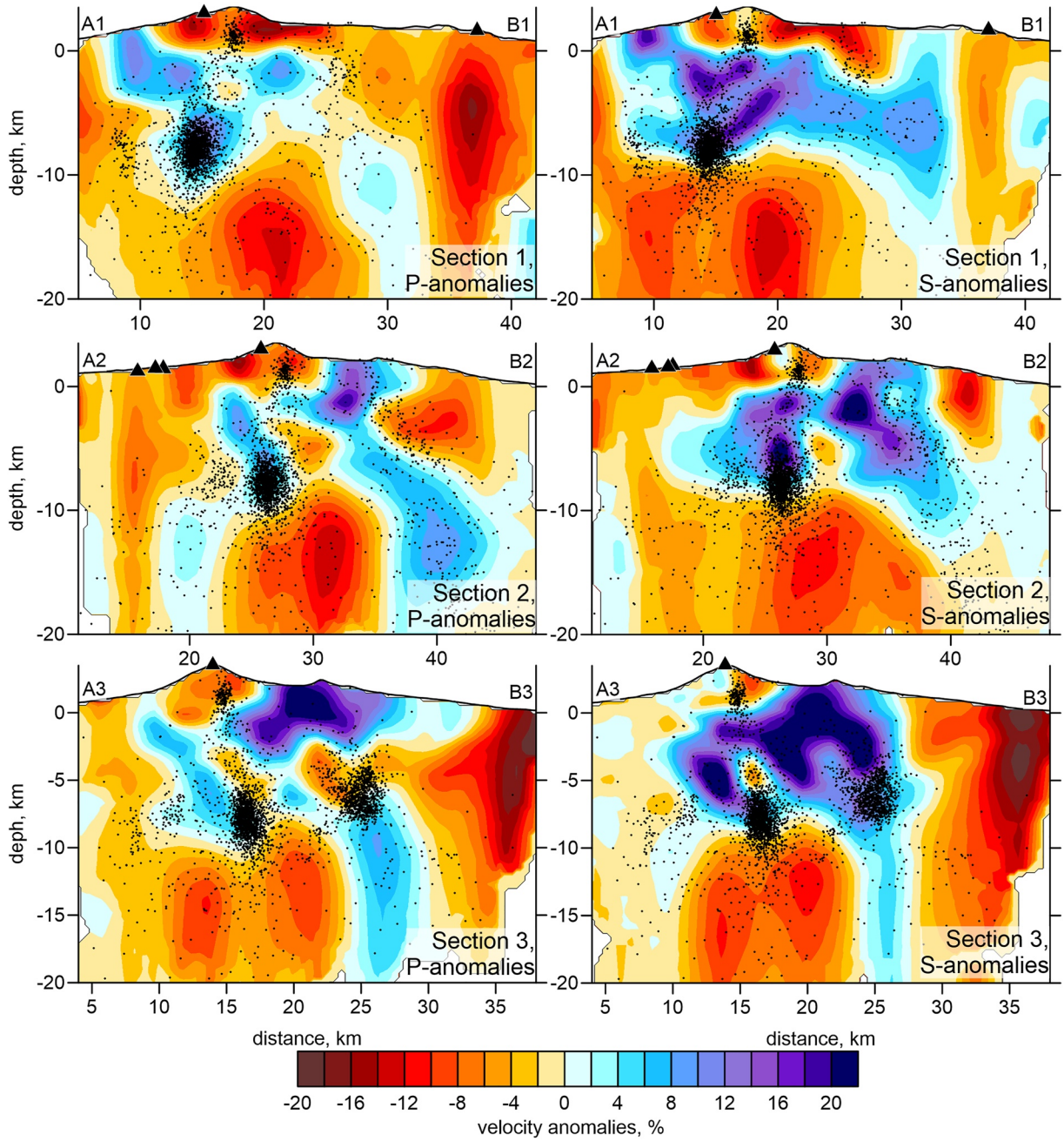

Figure 9. P and S wave velocity anomalies in three vertical sections whose locations are shown in Figure 6. The black dots indicate the projections of the events located at the distance of 3 km from the profile. The black triangles depict the projections of vents that produced historical lava flows.

local features in topography cannot be isostatically compensated for, and therefore give strong positive Bouger anomalies (e.g., the area around Elbrus volcano in northern Caucasus; Zaalishvili et al., 2015). In the case of Tenerife, the crust is oceanic and, around the island, has a thickness of ~10 km (De Barros et al., 2012; Lodge et al., 2012). Tectonic and volcanic processes have weakened the crust, making it more susceptible to vertical displacement. Based on apparent changes in absolute velocity, we suggest that isostatic displacement occurs along steep faults coinciding with the caldera limits (dotted lines in Figures 9 and 10). Such strong variation of crustal depth is generally supported by the receiver function analysis of Lodge et al. (2012), who estimated 1D velocity distributions for selected parts of Tenerife. Similar to our findings, they reported a velocity jump at ~17 km depth below the Las Cañadas caldera, much shallower than high-gradient velocity zones beneath other

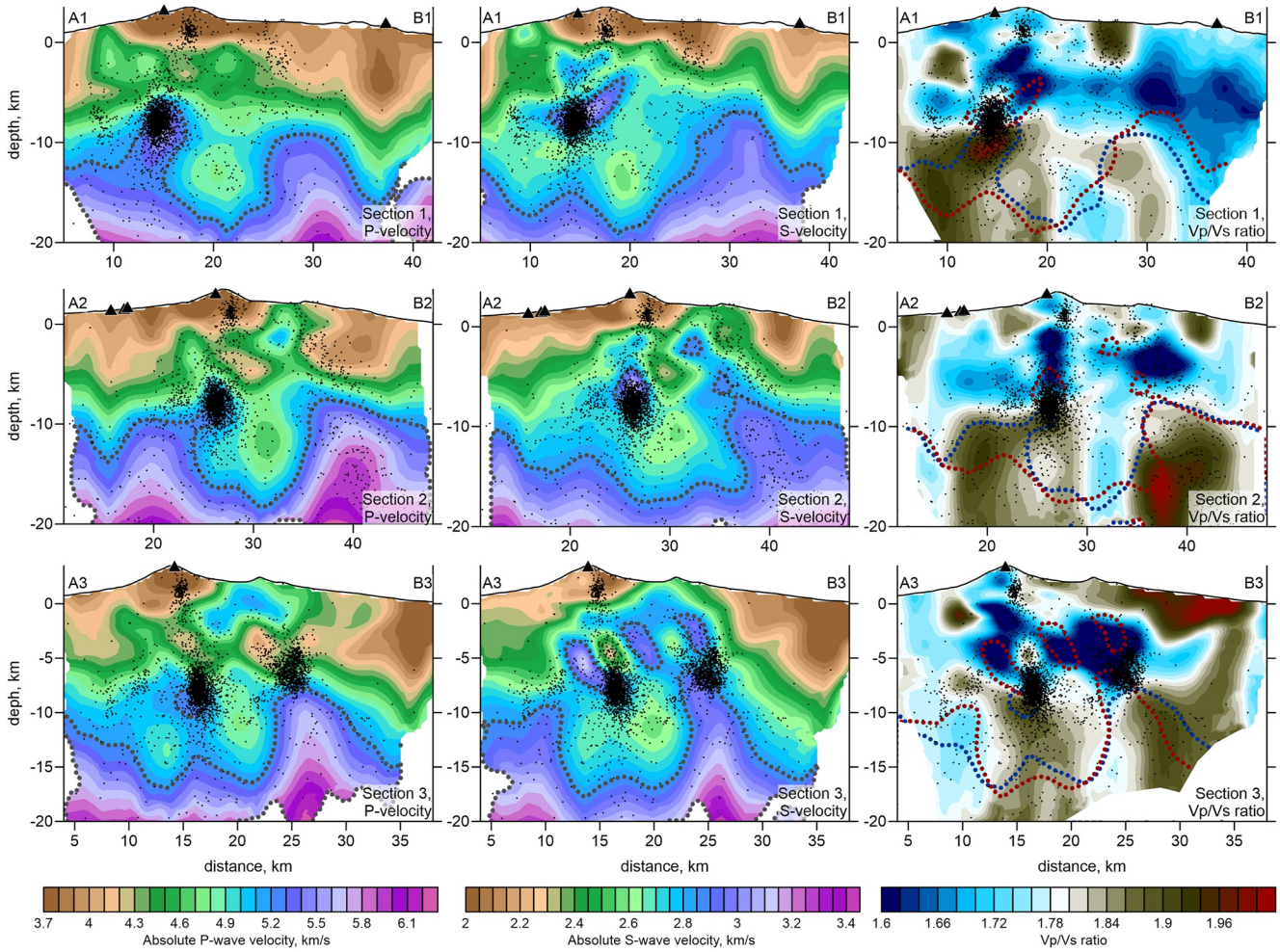

Figure 10. Absolute P and S wave velocities and the Vp/Vs ratio in three vertical sections whose positions are shown in Figure 6. The black dots indicate the projections of the events located at the distance of 3 km from the profile. The dotted lines indicate the contour lines of 5.2 km/s and 2.85 km/s of the P and S wave velocities, respectively. In the sections with Vp/Vs ratio, the same contours are indicated with the blue and red contour limes, respectively. The black triangles depict the projections of vents that produced historical lava flows.

parts of the island. It should be noted, however, that such strong contrasts in crustal thickness may result in unstable receiver function solutions (Lodge et al., 2012).

From Figures 11b and 12b, thinner parts of the crust are underlain by pockets of high *Vp/Vs*, which we interpret as large mafic magma reservoirs permanently stored below the crustal bottom. These anomalies are located below the areas of recent basaltic fissure volcanism along the radial ridges. We schematically draw a system of fractures and dykes that episodically deliver magma from these sub-crustal mafic reservoirs to the surface. As such, magma erupted at the surface arrives directly from the mantle, it has undergone little or no chemical transformation or fractionation.

We observed a prominent anomaly of low *Vp*, low *Vs*, and relatively high *Vp/Vs* at ~5 km b.s.l. beneath the center of the Las Cañadas caldera; we interpret this as the reservoir of phonolitic magma (highlighted by red and indicated by "Pho" in Figures 11 and 12). Just below the volcano edifice, at approximately sea level, we observed smaller anomalies with the same characteristics (also indicated by "Pho"), which we interpret as the shallow-most magma sources directly responsible for phonolitic eruptions inside the caldera. The locations of these magma sources are consistent with the results of petrological studies, which indicate that the Teide and Pico Viejo feeding reservoirs are located at depths of 4–5 km below surface, while those of Montaña Blanca and Roques Blancos are 1–2 km below the surface (Andújar & Scaillet, 2012; Andujar et al., 2013). In addition, previous studies of scattered waves (Del Pezzo et al., 1997) and seismic arrays (Almendros et al., 2000) have found evidence for

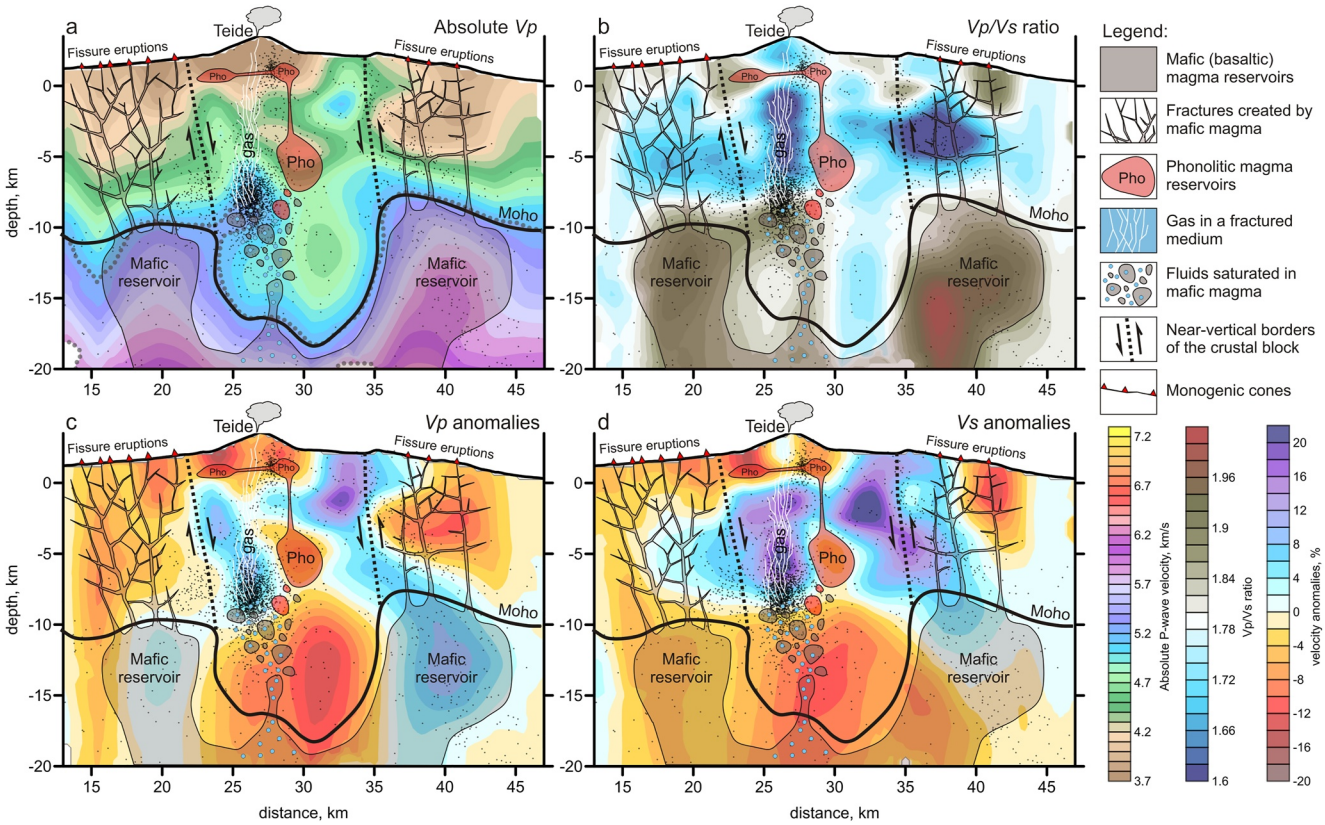

Figure 11. Interpretation of the tomography results in Section 2 based on: (a) Absolute P-wave velocity, (b) Vp/Vs ratio, (c) P-wave velocity anomalies and (d) S-wave velocity anomalies. Detailed description of the model is presented in the text.

several shallow fracture conduits and the presence of strong shallow scatters, probably related to the presence of heterogeneities with high velocity contrasts; these features affect seismic wave propagation owing to strong conversion of seismic waves from pure S-type to mixed surface waves. Our interpretation is corroborated by recent petrological studies of the same region. Horn et al. (2022) present new evidence of several mafic/intermediate melt structures along with the existence of a phonolitic magma structure below the Las Cañadas caldera.

As shown in Figures 11 and 12, a prominent columnar anomaly of high *Vp*, high *Vs*, and low *Vp/Vs* extends to ~7 km b.s.l., directly below Teide; this zone is characterized by a dense cluster of seismicity, which was coincident with a significant increase of fumarole activity in the Teide crater. We suggest that this anomaly represents a brittle zone where degassed fluids form fractures and quickly propagate upwards (white lines indicated by "gas").

Based on our findings, we propose a schematic representation (Figure 13) of volcanic and tectonic activity in Tenerife. The oceanic crust beneath most parts of Tenerife is ~10 km thick and has predominantly brittle characteristics. Therefore, high-pressure sub-crustal basalts can easily create hydro-fractures that quickly transport magma to the surface, where it feeds regular fissure eruptions. At the same time, the central part of the island has a considerably larger Moho interface depth, reaching up to 18 km. Such crust can no longer be considered oceanic, and is better described as in transition to continental type. This block has a relatively small horizontal extent and is approximately isometric in map view. The vertical deviation at the Moho interface is compatible with the lateral size of this flexure. In map view, the area of thickened crust traces the border of the Las Cañadas caldera, possibly indicating that they are linked. We suggest that the block behaves much like a press-button, representing a cylinder moving easily in the vertical direction. As it marks the triple junction between the volcanic ridges, the central part of the island is affected by the most intensive volcanic activity, which provides continuous growth and high topography, reaching 2,500 m in the pre-caldera era (Hurlimann et al., 1999) and 3,715 m today (at the summit of Teide). Therefore, in addition to a caldera-forming eruption and/or huge landslide (e.g., Brown & Branney, 2004), isostatic compensation is another possible mechanism of caldera subsidence.

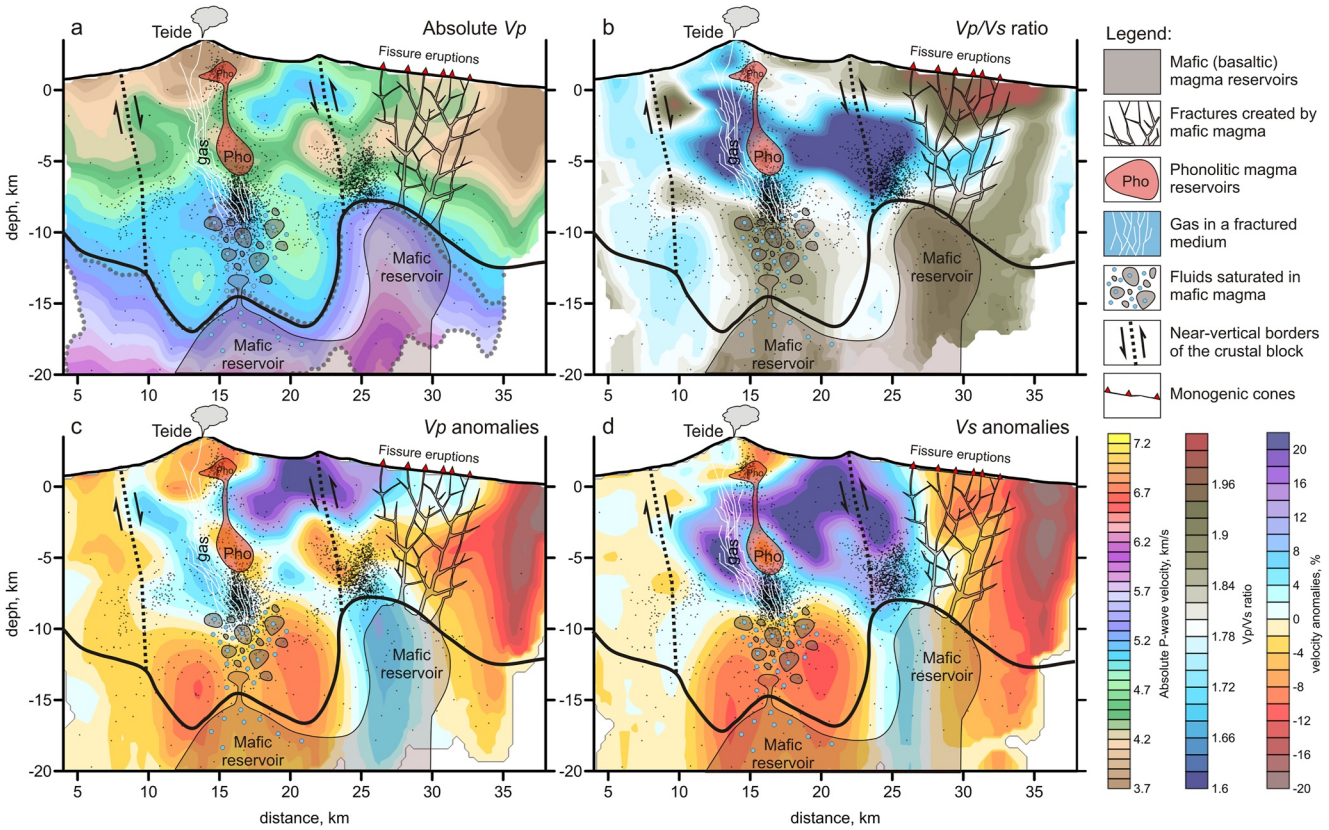

Figure 12. Same as Figure 11, but for Section 3.

The central crustal block has different seismic properties to the surrounding areas, which is consistent with the differences in volcanic activity. In areas of thinner crust, fissure basaltic volcanism is typical of most hotspot islands. The central block represents transitional crust, in which magmas undergo slow evolution. In our tomography model, we observed a high *Vp/Vs* ratio anomaly in the lower part of the "keel", which may represent slow ascent of fluid-saturated magma in a ductile medium, compatible with the petrological model of Horn et al. (2022). At some point, oversaturation reaches a threshold, causing abrupt fluid release and degassing. We suggest that this process was the cause of the seismic swarm observed after 2017. Such activity has the potential to impact on phonolitic reservoirs below the caldera, and may lead to new felsic eruptions.

For El Hierro, the tomography model of García-Yeguas et al. (2014) revealed a high-velocity consolidated crustal block underlying most of the island. During a strong seismic crisis in 2011–2012, most earthquakes occurred at 10–12 km depth, just below the central part of this block. García-Yeguas et al. (2014) suggested that this seismicity marked an activated magma attempting to exit its reservoir. As El Hierro is a relatively small island, the magma could bypass the rigid block, and travel through weaker surrounding rocks. As a result, seismicity moved from the central part of El Hierro to its margin, and finally resulted in a relatively weak submarine eruption in an offshore area. Owing to the larger size of the island, magma transport beneath Tenerife remains onshore.

La Palma, which had a strong effusive eruption in September–November 2021, offers a case study that is more similar to Tenerife. A recent seismic tomography model shows a distinct boundary at ~10 km depth, representing the Moho interface (D'Auria et al., 2022). Before the eruption, seismic activity occurred only in the mantle, indicating that deep magma reservoirs were episodically activated over several years. However, in early September 2021, the pressure overcame a level corresponding to the rigidity of the crust and created a pathway for magma ascent to the surface. The resemblance of structures beneath La Palma and Tenerife makes it possible the occurrence of eruptions on Tenerife in a similar manner as was recently in La Palma.

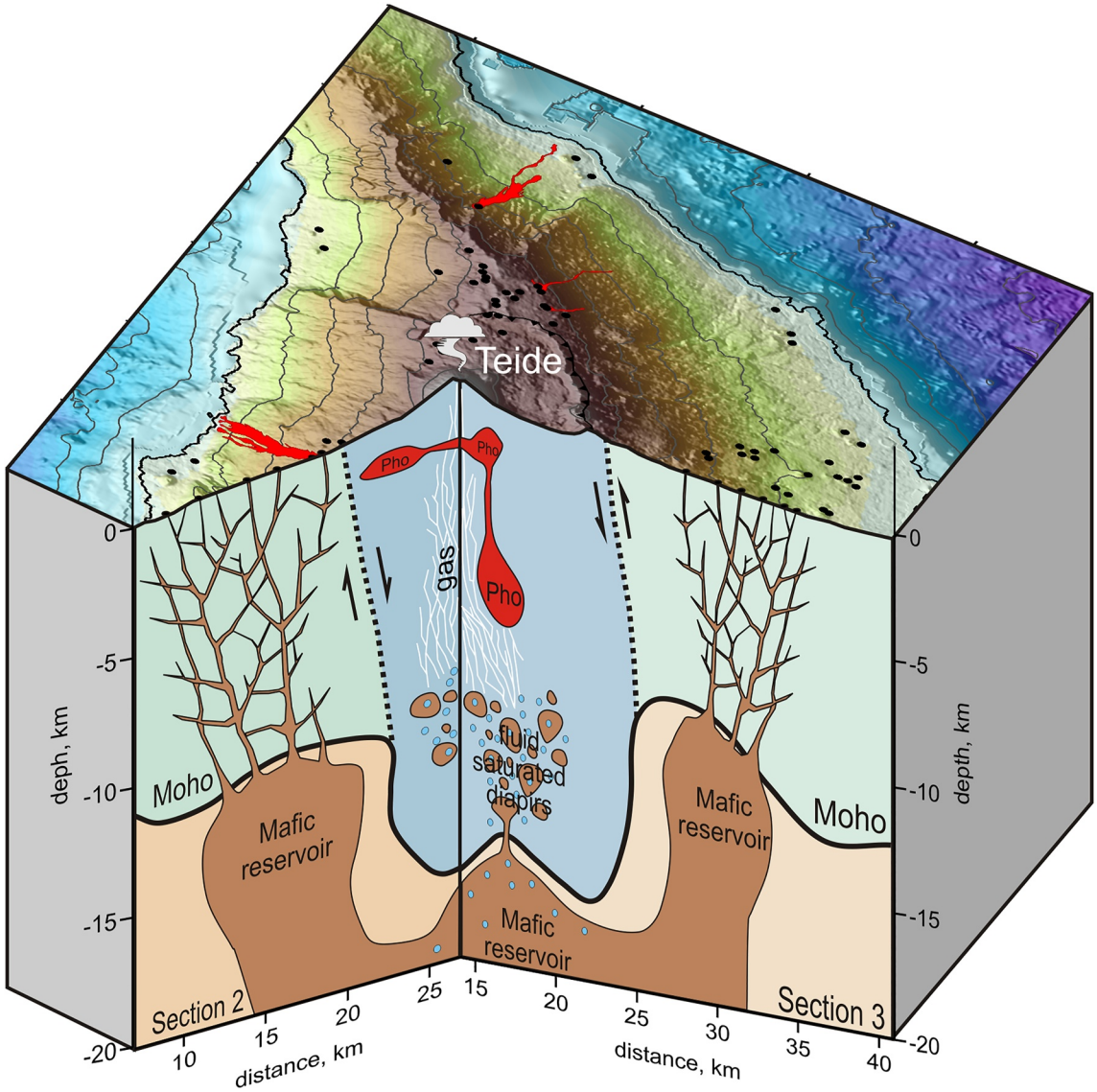

Figure 13. Conceptual model with the main elements of crustal structure and magma plumbing system according to the interpretation for Sections 2 and 3 given in Figures 11 and 12. The indications are the same as in the Legend in Figures 11 and 12.

6. Conclusions

We performed a passive source tomography inversion for Tenerife Island based on the *P*- and *S*-waves arrival times of local seismicity. For the first time, we jointly obtained the distributions of *P*- and *S*-wave velocities (*Vp* and *Vs*) and the locations of earthquakes. The dense distributions of seismic stations and large number of events allowed for high-resolution velocity models down to ∼20 km depth, as confirmed by synthetic modeling.

Consistent with previous studies of Tenerife, our model shows high velocity in the upper crust beneath the central part of the island, which may represent a rigid core of the volcanic complex consisting of igneous rocks. At greater depths below the Las Cañadas caldera, we observed prominent low *Vp* and low *Vs* anomalies, which may represent local crustal thickening. These observations reveal a unique situation: very strong crustal thickening from 10 to 17 km depth with a relatively limited horizontal extent (∼10 km across) and elliptical shape that roughly coincides with the limits of the Las Cañadas caldera. We suggest that the area below the caldera behaves as a press-button, isostatically moving in the vertical direction when non-compensated masses are emplaced. The central part of the island where this block is located is situated at the junction of three rift zones and, therefore, experiences the highest intensity of volcanic activity. Erupted materials cause active topographic growth, which

is isostatically compensated for by thick roots at the base of the crust. The mechanism of such strong isostatic compensation in such a small area is not clearly understood and requires further investigations (e.g., geomechanical modeling).

Below thinner parts of the crust, high *Vp/Vs* anomalies may represent reservoirs of mafic mantle melt. As the location of these anomalies coincides with the distributions of cinder cones, we suggest that they are connected to the surface by a system of fractures, and are responsible for the basaltic fissure eruptions occurring along the three radial rift zones on Tenerife.

At 5 km beneath the center of the Las Cañadas caldera, our tomography model reveals an anomaly interpreted to represent an intermediate reservoir of phonolite magmas. At approximately sea level (2–3 km below the surface of the Teide and Pico Viejo volcanoes), two smaller seismic anomalies may represent shallow magma reservoirs that are directly responsible for recent explosive eruptions in these areas.

Conflict of Interest

The authors declare no conflicts of interest relevant to this study.

Data Availability Statement

Derived products from this publication, including travel times of *P*- and *S*-waves and the full folder of the LOTOS code are presented in the file repository: Koulakov Ivan. (2022). Data and program codes to reproduce the results of local earthquake seismic tomography for Tenerife Island can be found at https://doi.org/10.5281/zenodo.7128756. Data from the IGN catalogue are available at https://doi.org/10.7419/162.03.2022.
The digital elevation model and historical lava flows were downloaded from the public graphic repository of GrafCan (www.grafcan.es). The software used to generate Figure 1 was QGIS 3.22 (https://www.qgis.org). Lotos software was used to generate Figures 2–8.

Acknowledgments
We are specially grateful to the editor Michael Bostock, the associate Editor Greg Waite and two anonymous reviewers for their insightful comments and suggestions, which significantly improved this manuscript. IK was supported by the Russian Science Foundation (Grant 20-17-00075). The INVOLCAN team was supported by the projects VOLRISKMAC II (MAC2/3.5b/328) and co-financed by the Interreg-MAC EU program TFvolcano projects, financed by the Instituto Tecnológico y de Energías Renovables (ITER). JP and JMI were partially supported by the Spanish FEMALE project (PID2019-106260GB-I00) and PROOF-FOREVER project. SA was supported by the project FWZZ-2022.0017. We also acknowledge Rubén García-Hernández, David Martínez van Dorth, Victor Ortega, Monika Przeor, and the countless persons who contributed to the seismic data analysis and the maintenance of the seismic network of Tenerife. Funding for open access charge: Universidad de Granada/CBUA. English language editing was performed by Tornillo Scientific, UK.

References

Ablay, G. J., Ernst, G. G. J., Martí, J., & Sparks, R. S. J. (1995). The 2 ka subplinian eruption of Montaña Blanca, Tenerife. *Bulletin of Volcanology*, *57*(5), 337–355. https://doi.org/10.1007/BF00301292

Ablay, G. J., & Martí, J. (2000). Stratigraphy, structure and volcanic evolution of the Pico Teide-Pico Viejo formation, Tenerife, Canary Islands. *Journal of Volcanology and Geothermal Research*, *103*(1–4), 175–208. https://doi.org/10.1016/S0377-0273(00)00224-9

Albert-Beltran, J. F., Arana, V., Diez, J. L., & Valentin, A. (1990). Physical-chemical conditions of the Teide volcanic system (Tenerife, Canary Islands). *Journal of Volcanology and Geothermal Research*, *43*(1–4), 321–332. https://doi.org/10.1016/0377-0273(90)90059-o

Almendros, J., Ibáñez, J. M., Alguacil, G., Morales, J., Del Pezzo, E., La Rocca, M., et al. (2000). A double seismic antenna experiment at Teide volcano: Existence of local seismicity and lack of evidences of volcanic tremor. *Journal of Volcanology and Geothermal Research*, *103*(1–4), 439–462. https://doi.org/10.1016/s0377-0273(00)00236-5

Almendros, J., Ibáñez, J. M., Carmona, E., & Zandomeneghi, D. (2007). Array analyses of volcanic earthquakes and tremor recorded at Las Cañadas caldera (Tenerife Island, Spain) during the 2004 seismic activation of Teide volcano. *Journal of Volcanology and Geothermal Research*, *160*(3–4), 285–299. https://doi.org/10.1016/j.jvolgeores.2006.10.002

Amonte, C., Asensio-Ramos, M., Melián, G. V., Pérez, N. M., Padrón, E., Hernández, P. A., et al. (2021). Hydrogeochemical temporal variations related to changes of seismic activity at Tenerife, Canary Islands. *Bulletin of Volcanology*, *83*(4), 1–18. https://doi.org/10.1007/s00445-021-01445-4

Amonte, C., Pérez, N. M., Melián, G. V., Asensio-Ramos, M., Padrón, E., & Hernández, P. A. (2022). Temporal evolution of dissolved gases in groundwater of Tenerife Island. *Journal of Volcanology and Geothermal Research*, *424*, 107512. https://doi.org/10.1016/j.jvolgeores.2022.107512

Ancochea, E., Fuster, J., Ibarrola, E., Cendrero, A., Coello, J., Hernan, F., et al. (1990). Volcanic evolution of the island of Tenerife (Canary Islands) in the light of new K-Ar data. *Journal of Volcanology and Geothermal Research*, *44*(3–4), 231–249. https://doi.org/10.1016/0377-0273(90)90019-C

Ancochea, E., Huertas, M. J., Cantagrel, J. M., Coello, J., Fúster, J. M., Arnaud, N., & Ibarrola, E. (1999). Evolution of the Cañadas edifice and its implications for the origin of the Cañadas Caldera (Tenerife, Canary Islands). *Journal of Volcanology and Geothermal Research*, *88*(3), 177–199. https://doi.org/10.1016/s0377-0273(98)00106-1

Andújar, J., Costa, F., & Scaillet, B. (2013). Storage conditions and eruptive dynamics of central versus flank eruptions in volcanic islands: The case of Tenerife (Canary Islands, Spain). *Journal of Volcanology and Geothermal Research*, *260*, 62–79. https://doi.org/10.1016/j.jvolgeores.2013.05.004

Andújar, J., & Scaillet, B. (2012). Experimental constraints on parameters controlling the difference in the eruptive dynamics of phonolitic magmas: The case of Tenerife (Canary Islands). *Journal of Petrology*, *53*(9), 1777–1806. https://doi.org/10.1093/petrology/egs033

Anguita, F., & Hernán, F. (2000). The Canary Islands origin: A unifying model. *Journal of Volcanology and Geothermal Research*, *103*(1–4), 1–26. https://doi.org/10.1016/s0377-0273(00)00195-5

Araña, V., Camacho, A. G., Garcia, A., Montesinos, F. G., Blanco, I., Vieira, R., & Felpeto, A. (2000). Internal structure of Tenerife (Canary Islands) based on gravity, aeromagnetic and volcanological data. *Journal of Volcanology and Geothermal Research*, *103*(1–4), 43–64. https://doi.org/10.1016/s0377-0273(00)00215-8

Blanco-Montenegro, I., Nicolosi, I., Pignatelli, A., Garcıa, A., & Chiappini, M. (2011). New evidence about the structure and growth of ocean island volcanoes from aeromagnetic data: The case of Tenerife, Canary Islands. *Journal of Geophysical Research: Solid Earth*, *116*(B3), B03102. https://doi.org/10.1029/2010jb007646

Booth, B. (1973). The Granadilla pumice deposits of southern Tenerife, Canary Islands. *Proc. Geologist Assoc.*, *84*(3), 353–IN5. https://doi.org/10.1016/s0016-7878(73)80039-2

Brown, R. J., & Branney, M. J. (2004). Bypassing and diacrinous deposition from density currents: Evidence from a giant regressive bed form in the poris ignimbrite, Tenerife, Canary Islands. *Geology*, *32*(5), 445–448. https://doi.org/10.1130/g20188.1

Bryan, S. E., Martí, J., & Cass, R. A. F. (1998). Stratigraphy of the bandas del sur formation: An extracaldera record of quaternary phonolitic explosive eruptions from the las Canada's edifice, Tenerife (Canary Islands). *Geological Magazine*, *135*(05), 605–636. https://doi.org/10.1017/s0016756897001258

Bushenkova, N., Koulakov, I., Senyukov, S., Gordeev, E. I., Huang, H.-H., El-Khrepy, S., & Al-Alarifi, N. (2019). Tomographic images of magma chambers beneath the Avacha and Koryaksky volcanoes in Kamchatka. *Journal of Geophysical Research: Solid Earth*, *124*(9), 9694–9713. https://doi.org/10.1029/2019JB017952

Camacho, A. G., Fernández, J., & Gottsmann, J. (2011). The 3-D gravity inversion package GROWTH2.0 and its application to Tenerife Island, Spain. *Computers and Geosciences*, *37*(4), 621–633. https://doi.org/10.1016/j.cageo.2010.12.003

Camacho, A. G., Vieir, R., & De Toro, C. (1991). Microgravimetric model of the las Cañadas caldera (Tenerife). *Journal of Volcanology and Geothermal Research*, *47*(1–2), 75–88. https://doi.org/10.1016/0377-0273(91)90102-6

Canales, J. P., Dañobeitia, J. J., & Watts, A. B. (2000). Wide-angle seismic constraints on the internal structure of Tenerife, Canary Islands. *Journal of Volcanology and Geothermal Research*, *103*(1–4), 65–81. https://doi.org/10.1016/s0377-0273(00)00216-x

Canas, J., Ugalde, A., Pujades, L., Carracedo, J., Soler, V., & Blanco, M. (1998). Intrinsic and scattering seismic wave attenuation in the Canary Islands. *Journal of Geophysical Research*, *103*(B7), 15037–15050. https://doi.org/10.1029/98JB00769

Cantagrel, J. M., Arnaud, N. O., Ancochea, E., Fúster, J. M., & Huertas, M. J. (1999). Repeated debris avalanches on Tenerife and Genesis of las Cañadas caldera wall (Canary Islands). *Geology*, *27*(8), 739–742. https://doi.org/10.1130/0091-7613(1999)027<0739:rdaota>2.3.co;2

Carracedo, J. C., Badiola, E. R., Guillou, H., Paterne, M., Scaillet, S., Torrado, F. P., et al. (2007). Eruptive and structural history of Teide volcano and rift zones of Tenerife, Canary Islands. *Geological Society of America Bulletin*, *119*(–10), 1027–1051. https://doi.org/10.1130/b26087.1

Carracedo, J. C., & Perez-Torrado, F. J. (2013). Geological and geodynamic context of the Teide volcanic complex. In J. C. Carracedo & V. R. Troll (Eds.), *Teide Volcano* (pp. 23–36). Springer. https://doi.org/10.1007/978-3-642-25893-0_2

Carracedo, J. C., Perez-Torrado, F. J., Rodriguez-Gonzalez, A., Fernandez-Turiel, J. L., Klügel, A., Troll, V. R., & Wiesmaier, S. (2012). The ongoing volcanic eruption of El Hierro, Canary Islands. *Eos Transactions American Geophysical Union*, *93*(9), 89–90. https://doi.org/10.1029/2012eo090002

Carracedo, J. C., & Troll, V. R. (2013). Structural and geological elements of Teide Volcanic complex: Rift zones and gravitational collapses. In J. C. Carracedo & V. R. Troll (Eds.), *Teide Volcano* (pp. 57–74). Springer. https://doi.org/10.1007/978-3-642-25893-0_4

Coppo, N., Schnegg, P., Heise, W., Falco, P., & Costa, R. (2008). Multiple caldera collapses inferred from the shallow electrical resistivity signature of the las Cañadas Caldera, Tenerife Canary Islands. *Journal of Volcanology and Geothermal Research*, *170*(3–4), 153–166. https://doi.org/10.1016/j.jvolgeores.2007.09.013

Coppo, N., Schnegg, P. A., Falco, P., & Costa, R. (2010). Conductive structures around Las Cacadas caldera, Tenerife (Canary Islands, Spain): A structural control. *Geológica Acta*, *8*(1), 67–82. https://doi.org/10.1344/105.000001516

D'Auria, L., Barrancos, J., Padilla, G. D., Perez, N. M., Hernandez, P. A., Melian, G., et al. (2019). The 2016 Tenerife (Canary Islands) long-period seismic swarm. *Journal of Geophysical Research*, *124*(8), 8739–8752. https://doi.org/10.1029/2019JB017871

D'Auria, L., Koulakov, I., Prudencio, J., Cabrera-Pérez, I., Barrancos, J., García-Hernández, R., et al. (2022). Voluminous storage and rapid magma ascent beneath La Palma revealed by seismic tomography. *Scientific Reports*, *12*(1), 17654. https://doi.org/10.1038/s41598-022-21818-9

De Barros, L., Martini, F., Bean, C. J., Garcia-Yeguas, A., & Ibanez, J. (2012). Imaging magma storage below Teide volcano (Tenerife) using scattered seismic wavefields. *Geophysical Journal International*, *191*(2), 695–706. https://doi.org/10.1111/j.1365-246X.2012.05637.x

Del Pezzo, E., La Rocca, M., & Ibanez, J. (1997). Observations of high-frequency scattered waves using dense arrays at Teide volcano. *Bulletin of the Seismological Society of America*, *87*(6), 1637–1647. https://doi.org/10.1785/bssa0870061637

Di Stefano, R., Kissling, E., Chiarabba, C., Amato, A., & Giardini, D. (2009). Shallow subduction beneath Italy: Three-dimensional images of the Adriatic-European-Tyrrhenian lithosphere system based on high-quality P wave arrival times. *Journal of Geophysical Research: Solid Earth*, *114*(B5), B05305. https://doi.org/10.1029/2008jb005641

Dóniz, J., Romero, C., Coello, E., Guillén, C., Sánchez, N., García-Cacho, L., & García, A. (2008). Morphological and statistical characterization of recent mafic volcanism on Tenerife (Canary Islands, Spain). *Journal of Volcanology and Geothermal Research*, *173*(3–4), 185–195. https://doi.org/10.1016/j.jvolgeores.2007.12.046

Eberhart-Phillips, D. (1993). Local earthquake tomography: Earthquake source regions. In H. M. Iyer & K. Hirahara (Eds.), *Seismic tomography: Theory and Practice* (pp. 613–643). Chapman and Hall.

Edgar, C. J., Wolff, J. A., Olin, P. H., Nichols, H. J., Pittari, A., Cas, R. A. F., et al. (2007). The late quaternary Diego Hernandez Formation, Tenerife: Volcanology of a complex cycle of voluminous explosive phonolitic eruptions. *Journal of Volcanology and Geothermal Research*, *160*(1–2), 59–85. https://doi.org/10.1016/j.jvolgeores.2006.06.001

García-Yeguas, A., Ibáñez, J. M., Koulakov, I., Jakovlev, A., Romero-Ruiz, C. M., & Prudencio, J. (2014). Seismic tomography model reveals mantle magma sources of recent volcanic activity at El Hierro Island (Canary Islands, Spain). *Geophysical Journal International*, *199*(3), 1739–1750. https://doi.org/10.1093/gji/ggu339

García-Yeguas, A., Koulakov, I., Ibáñez, J. M., & Rietbrock, A. (2012). High resolution 3D P wave velocity structure beneath Tenerife Island (Canary Islands, Spain) based on tomographic inversion of active-source data. *Journal of Geophysical Research: Solid Earth*, *117*(B9). https://doi.org/10.1029/2011jb008970

Global Volcanism Program. (2013). Tenerife (383030) in volcanoes of the world, v. 4.10.6 (24 Mar 2022). In E. Venzke (Ed.), *Smithsonian institution*. Retrieved from https://volcano.si.edu/volcano.cfm?vn=383030

Gottsmann, J., Camacho, A. G., Martí, J., Wooller, L., Fernández, J., García, A., & Rymer, H. (2008). Shallow structure beneath the central volcanic complex of Tenerife from new gravity data: Implications for its evolution and recent reactivation. *Physics of the Earth and Planetary Interiors*, *168*(3–4), 212–230. https://doi.org/10.1016/j.pepi.2008.06.020

Horn, E. L., Taylor, R. N., Gernon, T. M., Stock, M. J., & Farley, E. M. R. (2022). Composition and petrology of a mush-bearing magma reservoir beneath Tenerife. *Journal of Petrology*, *63*(10). egac095. https://doi.org/10.1093/petrology/egac095

Hurlimann, M., Turon, E., & Martí, J. (1999). Large landslides triggered by caldera collapse events in Tenerife, Canary Islands. *Physics and Chemistry of the Earth A Solid Earth Geophysics*, *24*(10), 921–924. https://doi.org/10.1016/S1464-1895(99)00136-2

Ibáñez, J. M., Rietbrock, A., & García-Yeguas, A. (2008). Imaging an active volcano edifice at Tenerife Island, Spain. *Eos Transactions American Geophysics Union*, *89*(32), 289. https://doi.org/10.1029/2008eo320001
Khrepy, S., Koulakov, I., & Al-Arifi, N. (2016). Crustal structure beneath the continental rifting area of Gulf of Suez from earthquakes tomography. *Tectonophysics*, *668–669*, 92–104. https://doi.org/10.1016/j.tecto.2015.11.027
Kissling, E., Ellsworth, W. L., Eberhart-Phillips, D., & Kradolfer, U. (1994). Initial reference models in local earthquake tomography. *Journal of Geophysical Research*, *99*(B10), 19635–19646.
Koulakov, I. (2009). LOTOS code for local earthquake tomographic inversion: Benchmarks for testing tomographic algorithms. *Bulletin of the Seismological Society of America*, *99*(1), 194–214. https://doi.org/10.1029/93jb03138
Koulakov, I. (2020). Basic TOMO: An educational tool for investigating the role of controlling parameters and observation geometry in tomography problems. *Geophysical Technologies*, *1*, 40–54. https://doi.org/10.18303/2619-1563-2020-1-40
Koulakov, I., Boychenko, E., & Smirnov, S. Z. (2020). Magma chambers and meteoric fluid flows beneath the Atka volcanic complex (Aleutian Islands) inferred from local earthquake tomography. *Geosciences*, *10*(6), 214. https://doi.org/10.3390/geosciences10060214
Koulakov, I., Maksotova, G., Mukhopadhyay, S., Raoof, J., Kayal, J. R., Jakovlev, A., & Vasilevsky, A. N. (2015). Variations of the crustal thickness in Nepal Himalayas based of tomographic inversion of regional earthquake data. *Solid Earth*, *6*(1), 207–216. https://doi.org/10.5194/se-6-207-2015
Koulakov, I., Plechov, P., Mania, R., Walter, T. R., Smirnov, S. Z., Abkadyrov, I., et al. (2021). Anatomy of the Bezymianny volcano merely before an explosive eruption on 20.12.2017. *Scientific Reports*, *11*(1), 1758. https://doi.org/10.1038/s41598-021-81498-9
Lodge, A., Nippress, S. E. J., Rietbrock, A., García-Yeguas, A., & Ibáñez, J. M. (2012). Evidence for magmatic underplating and partial melt beneath the Canary Islands derived using teleseismic receiver functions. *Physics of the Earth Planetary Interiors*, *212*, 44–54. https://doi.org/10.1016/j.pepi.2012.09.004
Longpré, M. A. (2021). Reactivation of Cumbre Vieja volcano. *Science*, *374*(6572), 119–1198. https://doi.org/10.1126/science.abm9423
Martí, J. (2019). Las Cañadas caldera, Tenerife, Canary Islands: A review, or the end of a long volcanological controversy. *Earth-Science Reviews*, *196*, 102889. https://doi.org/10.1016/j.earscirev.2019.102889
Martí, J., & Gudmundsson, A. (2000). The las Cañadas caldera (Tenerife, Canary Islands): An overlapping collapse caldera generated by magma-chamber migration. *Journal of Volcanology and Geothermal Research*, *103*(1–4), 161–173. https://doi.org/10.1016/s0377-0273(00)00221-3
Martí, J., Hurlimann, M., Ablay, G. J., & Gudmundsson, A. (1997). Vertical and lateral collapses on Tenerife (Canary Islands) and other volcanic ocean islands. *Geology*, *25*(10), 879–882. https://doi.org/10.1130/0091-7613(1997)025<0879:valcot>2.3.co;2
Melian, G., Tassi, F., Perez, N., Hernandez, P., Sortino, F., Vaselli, O., et al. (2012). A magmatic source for fumaroles and diffuse degassing from the summit crater of Teide volcano (Tenerife, Canary Islands): A geochemical evidence for the 2004–2005 seismic–volcanic crisis. *Bulletin of Volcanology*, *74*(6), 1465–1483. https://doi.org/10.1007/s00445-012-0613-1
Mitjavila, J., & Villa, I. (1993). Temporal evolution of Diego Hernández formation las Cañadas, Tenerife and confirmation of the age of the Caldera using the 40Ar-39Ar method. *Revista de la Sociedad Geologica de Espana*, *6*, 61–65.
Nolet, G. (1987). Seismic wave propagation and seismic tomography. *Seismic Tomography*, 1–23. https://doi.org/10.1007/978-94-009-3899-1_1
Ortiz, R., Arana, V., Astiz, M., & Garcia, A. (1986). Magnetotelluric study of the Teide (Tenerife) and Timanfaya (Lanzarote) volcanic areas. *Journal of Volcanology and Geothermal Research*, *30*(3–4), 357–377. https://doi.org/10.1016/0377-0273(86)90061-2
Padrón, E., Pérez, N. M., Hernández, P. A., Melián, G., Asensio-Ramos, M., D'Auria, L., et al. (2021). Changes in diffuse degassing from the summit crater of Teide volcano (Tenerife, Canary Islands) prior to the 2016 Tenerife long-period seismic swarm. *Journal of Geophysical Research: Solid Earth*, *126*(3), e2020JB020318. https://doi.org/10.1029/2020jb020318
Paige, C. C., & Saunders, M. A. (1982). Lsqr: An algorithm for sparse linear equations and sparse least squares. *ACM Transactions on Mathematical Software(TOMS)*, *8*(2), 43–71. Retrieved from. https://doi.org/10.1145/355984.355989
Paris, R., Ramalho, R. S., Madeira, J., Ávila, S., May, S. M., Rixhon, G., et al. (2018). Mega-tsunami conglomerates and flank collapses of ocean island volcanoes. *Marine Geology*, *395*, 168–187. https://doi.org/10.1016/j.margeo.2017.10.004
Perez, N. M., Hernandez, P. A., Padron, E., Melian, G., Nolasco, D., Barrancos, J., et al. (2013). An increasing trend of diffuse CO_2 emission from Teide volcano (Tenerife, Canary Islands): Geochemical evidence of magma degassing episodes. *Journal of the Geological Society*, *170*(4), 585–592. https://doi.org/10.1144/jgs2012-125
Piña-Varas, P., Ledo, J., Queralt, P., Marcuello, A., Bellmunt, F., Hidalgo, R., & Messeiller, M. (2014). 3-D magnetotelluric exploration of Tenerife geothermal system (Canary Islands, Spain). *Surveys in Geophysics*, *35*(4), 1045–1064. https://doi.org/10.1007/s10712-014-9280-4
Piña-Varas, P., Ledo, J., Queralt, P., Marcuello, A., & Perez, N. (2018). On the detectability of Teide volcano magma chambers (Tenerife, Canary Islands) with magnetotelluric data. *Earth Planetary Space*, *70*(1), 1–11. https://doi.org/10.1186/s40623-018-0783-y
Pous, J., Heise, W., Schnegg, P., Munoz, G., Martí, J., & Soriano, C. (2002). Magnetotelluric study of the las Cañadas caldera (Tenerife, Canary Islands): Structural and hydrogeological implications. *Earth and Planetary Science Letters*, *204*(1–2), 249–263. https://doi.org/10.1016/s0012-821x(02)00956-1
Prudencio, J., Del Pezzo, E., García-Yeguas, A., & Ibáñez, J. M. (2013). Spatial distribution of intrinsic and scattering seismic attenuation in active volcanic islands–I: Model and the case of Tenerife island. *Geophysical Journal International*, *195*(3), 1942–1956. https://doi.org/10.1093/gji/ggt361
Prudencio, J., Ibáñez, J. M., Del Pezzo, E., Martí, J., García-Yeguas, A., & De Siena, L. (2015). 3D attenuation tomography of the volcanic island of Tenerife (Canary Islands). *Surveys in Geophysics*, *36*(5), 693–716. https://doi.org/10.1007/s10712-015-9333-3
Romero, C. (1992). *Estudio geomorfológico de los volcanes históricos de Tenerife* (p. 265). Cabildo Insular de Tenerife.
Vargas, C. A., Koulakov, I., Jaupart, C., Gladkov, V., Gomez, E., El-Khrepy, S., & Al-Arifi, N. (2017). Breathing of the Nevado del Ruiz volcano reservoir, Colombia, inferred from repeated seismic tomography. *Scientific Reports*, *7*(1), 46094. https://doi.org/10.1038/srep46094
Ward, S. N., & Day, S. (2001). Cumbre Vieja volcano—Potential collapse and tsunami at La Palma, Canary Islands. *Geophysical Research Letters*, *28*(17), 3397–3400. https://doi.org/10.1029/2001gl013110
Wolff, J. A., Grandy, J. S., & Larson, P. B. (2000). Interaction of mantle-derived magma with island crust? Trace element and oxygen isotope data from the Diego Hernandez formation, las Cañadas, Tenerife. *Journal of Volcanology and Geothermal Research*, *130*(1–4), 343–366. https://doi.org/10.1016/s0377-0273(00)00230-4
Zaalishvili, V. B., Nevskaya, N. I., Nevskii, L. N., & Shempelev, A. G. (2015). Geophysical fields above volcanic edifices in the North Caucasus. *Journal of Volcanology and Seismology*, *9*(5), 333–338. https://doi.org/10.1134/s0742046315050085